Energy Advances

ROYAL SOCIETY OF CHEMISTRY

REVIEW ARTICLE

View Article Online
View Journal | View Issue



Cite this: *Energy Adv.*, 2023, 2, 235

# Metal-doped nickel-based chalcogenides and phosphochalcogenides for electrochemical water splitting

Dmitrii A. Rakov [ab]

The rational design of an affordable, stable, and active electrocatalyst is essential for a sustainable hydrogen economy. Recently, great progress has been achieved with nickel-based chalcogenides and phosphochalcogenides for both hydrogen and oxygen evolution reactions, and the metal doping strategy has been demonstrated to have a substantial impact on the performance of electrocatalysts. Common approaches to simultaneously improve the intrinsic activity of nickel-based (phospho)-chalcogenides by metal doping and increase the active surface area of the electrocatalyst bring some challenges to deciding accurately whether metal doping will improve the electrocatalytic activity or not. This review highlights the influence of 3d block metal doping (Cu, Co, Fe and Mn) on the electrocatalytic performance of these phases with reference to the electronic structure of the materials. Such aspects as the electrical conductivity, hydrogen and oxygen intermediate adsorption mechanism, surface bifunctionality, role of chalcogenide/phosphochalcogenide surface functional groups, electrocatalytic stability and related changes upon metal doping are discussed in this review article. This work discusses current gaps that need to be filled to develop a systematic strategy in the modulation of the electronic/structural properties of metal-doped nickel-based (phospho)chalcogenides for their effective use in electrochemical water splitting.

Received 22nd June 2022,
Accepted 8th December 2022

DOI: 10.1039/d2ya00152g

rsc.li/energy-advances



[a] *Institute for Frontier Materials, Deakin University, Geelong, Victoria 3217, Australia. E-mail: dmitrii.rakov@research.deakin.edu.au*
[b] *ARC Centre of Excellence for Electromaterials Science (ACES), Deakin University, Burwood, Victoria 3125, Australia*

**Dmitrii A. Rakov**

*Dmitrii Rakov was awarded his PhD degree from Deakin University (Australia) in Prof. Maria Forsyth's group. He has worked in NASA Ames research centre with Dr John W. Lawson within Universities Space Research Association program. He is currently a postdoctoral research fellow at the University of Queensland (Australia) in Prof. Chengzhong Yu's group. His research focuses on computational/experimental electromaterials science, in particular, on the optimization of the charge transfer mechanism in energy storage and conversion devices.*

## Introduction

In recent years, great attention has been devoted to renewable energy sources (*e.g.* solar, wind, tidal, geothermal, *etc.*) due to rising concerns about the energy crisis, global warming and the related use of fossil fuels.[1–3] Among many, hydrogen, as a carbon-free and high energy density (146 kJ $g^{-1}$) source, has become the main candidate for future alternative fuels.[3] Nowadays, hydrogen is mainly produced in three ways, namely methane steam reforming, coal gasification, and water electrolysis. Water electrolysis is one of the most environmentally friendly means of hydrogen generation.[4] The current development of hydrogen production through water splitting at the industrial scale requires a non-expensive, robust, and efficient catalyst. A typical cell for electrochemical water splitting consists of electrodes performing two half-reactions, the oxygen evolution reaction (OER) at the cathode and the hydrogen evolution reaction (HER) at the anode.

$$4H^+(aq) + 4e^- \rightarrow 2H_2(g) \quad E = (-0.059pH)\ V\ vs.\ RHE\ (reduction) \quad (1)$$

$$H_2O \rightarrow O_2(g) + 4H^+(aq) + 4e^- \quad E = (1.23\ V - 0.059pH)\ V\ vs.\ RHE\ (oxidation) \quad (2)$$

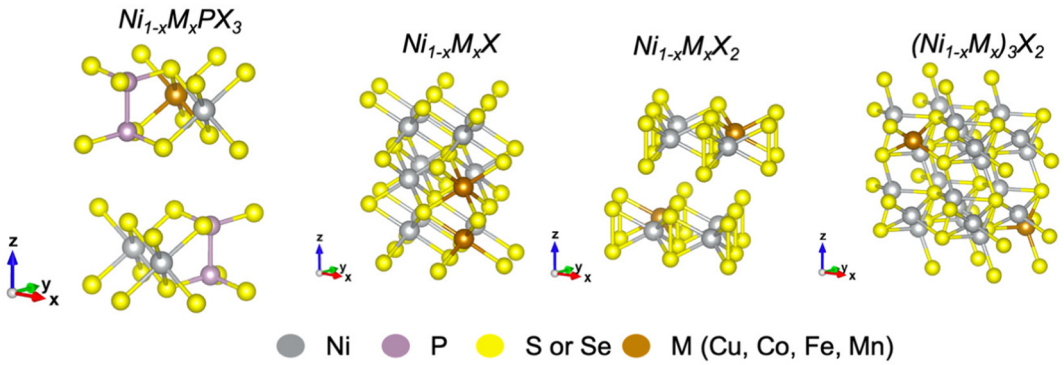


Fig. 1 Visual representation of unit cells for metal-doped (left) phosphochalcogenides (monoclinic, symmetry space group *P*1), nickel monochalcogenides (hexagonal, symmetry space group *P*1), nickel dichalcogenides (hexagonal, symmetry space group *P*1), and (right) tri nickel dichalcogenides (trigonal, symmetry space group *P*1). Axes *XYZ* correspond to periodic cell dimensions (ABC).

$$2H_2O \rightarrow O_2(g) + H_2(g) \quad \Delta E = 1.23\ V \qquad (3)$$

The HER is a process that reduces protons into hydrogen (reduces water to hydrogen from neutral/alkaline medium), while the OER process oxidizes water and hydroxyl anions to molecular oxygen from acid and neutral/alkaline medium.[5,6]

Recently, enormous progress has been made towards the development of a noble metal-free catalyst for electrochemical water splitting, though the underlying strategy for rational design and optimization of an affordable, stable and efficient electrocatalyst is still under development.[4,7–10] Multiple strategies have been suggested to improve the activity and stability of electrocatalysts, such as increasing the number of active sites, improving the intrinsic activity, and modifying the electrolyte composition.[11–17] The increase in the intrinsic activity of surface sites is a more effective means to optimize the overall activity of the electrocatalyst compared to the nanofabrication strategy.[11] The elemental doping has a significant impact on the overall electronic properties of the bulk phase as well as on the surface electrocatalytic activity.[17–24] Nickel-based transition metal chalcogenides ($M_aX_b$, where X = S, Se, Te) have been pointed out as promising noble-metal-free electrocatalysts for water splitting due to their high efficiency, tunable electrocatalytic behaviour, and reasonable cost of raw materials.[25–37] Another family of electrocatalysts such as transition metal phosphochalcogenides, *e.g.*, nickel phosphochalcogenides ($NiPX_3$, where X = S, Se), also so-called lamellar phases, consist of metal cation-supporting $[P_2S_6]^{4-}$ or $[P_2Se_6]^{4-}$ units weakly bonded to each other *via* van der Waals forces. These compounds are structurally similar to transition metal chalcogenides, and upon reduced dimensionality, they show a range of unique properties suitable for application in the electronic industry,[38,39] energy storage,[40–42] and catalysis;[31,43–45] more comprehensive reviews about the structure and application of $MPX_3$ materials can be found in the literature.[29,46,47]

Here, we summarize recent advances in transition metal (TM) doping of nickel chalcogenides and phosphochalcogenides for electrochemical water splitting. This review emphasizes the major aspects of elemental doping that should be considered for the rational optimization of the electrocatalytic activity and stability of catalysts for both the HER and OER. Fig. 1 shows unit cells of metal-doped nickel phosphochalcogenides and some typical nickel chalcogenides discussed in this review. To minimize the scope of this work, the review will consider only several 3d transition metals such as Cu, Co, Fe, and Mn.

## Mechanism of electrochemical water splitting and related factors

Regardless of the acidity of the electrolyte, the thermodynamic voltage for water splitting is 1.23 V at 25 °C and 1 atm. However, an extra potential, often referred to as an overpotential ($\eta$), is required to overcome activation energy barriers resulting from the additional resistance of the electrode, electrolyte and impurities (ions, dissolved gases), solid/gas interface and contacts resistance as the overall mechanism of the charge transfer at the electrocatalyst/electrolyte interface.[4,6,12,14,48–50] The reaction rate for both the HER and OER processes is greatly affected by the acidity of the electrolyte and the electrocatalyst nature.[51,52] Therefore, chemically and morphologically stable, and efficient noble-metal-free catalysts that can perform well towards both half-reactions in the same media are still highly required for electrochemical water splitting. Usually, the HER rate decreases in solutions with a high pH value due to the absence of free protons, while the electrocatalyst chemical stability, *e.g.*, against corrosion and elemental etching, and kinetics of the counter OER half-reaction are more efficient at higher pH due to partial surface oxidation and facile formation of oxygen intermediate species;[11,53–56] however, the water splitting mechanism in neutral and alkaline media is even more complex due to an extra step involving water dissociation. Recently, it was shown that not only the medium pH but also the electrode/electrolyte interfacial structure of solvated ions is important for the HER as it contributes to interfacial transport and the overall energy barrier for a conversion reaction, and therefore new strategies to optimize the arrangement of interfacial water molecules and their short-range order near the charged surface by tuning the cation chemistry should be considered.[57]

Table 1 Mechanism of the HER and OER in acidic aqueous media

| Step | HER in acid | OER in acid |
|---|---|---|
| Overall | $2H^+(aq) + 2e^- = H_2(g)$ | $2H_2O = 4H^+(aq) + O_2(g) + 4e^-$ |
| (1) | $H^+(aq) + e^- = H^*(ad)$ | $H_2O = OH(ad) + H^+(aq) + e^-$ |
| (2) | $H^+(aq) + e^- + H^*(ad) = H_2(g)$ | $OH(ad) = O(ad) + H^+(aq) + e^-$ |
| (3) | $H^*(ad) + H^*(ad) = H_2(g)$ | $O(ad) + H_2O = OOH(ad) + H^+(aq) + e^-$ |
| (4) | | $OOH(ad) = H^+(aq) + O_2(g) + e^-$ |

Table 2 Mechanism of the HER and OER in neutral/basic aqueous media

| Step | HER in neutral/alkaline | OER in neutral | OER in alkaline |
|---|---|---|---|
| Overall | $2H_2O + 2e^- = H_2(g) + 2OH^-(aq)$ | $4OH^-(aq) = 2H_2O + O_2(g) + 4e^-$ | $4OH^-(aq) = 2H_2O + O_2(g) + 4e^-$ |
| (1) | $H_2O + e^- = H^*(ad) + OH^-(aq)$ | $2H_2O = OH(ad) + H_2O + H^+(aq) + e^-$ | $OH^-(aq) = OH(ad) + e^-$ |
| (2) | $H_2O + e^- + H^*(ad) = H_2(g) + OH^-(aq)$ | $OH(ad) + H_2O = O(ad) + H_2O + H^+(aq) + e^-$ | $OH^-(aq) + OH(ad) = O(ad) + H_2O + e^-$ |
| (3) | $H^*(ad) + H^*(ad) = H_2(g)$ | $O(ad) + H_2O = OOH(ad) + H^+(aq) + e^-$ | $O(ad) + OH^-(aq) = OOH(ad) + e^-$ |
| (4) | | $OOH(ad) = H^+(aq) + O_2(g) + e^-$ | $OOH(ad) + OH^-(aq) = O_2(g) + H_2O + e^-$ |

The mechanism of electrochemical water splitting in different media is summarized in Tables 1 and 2.

The electrochemical catalyst minimizes the energy barrier to proceed through the chemical process compared to an identical non-catalytic reaction that does not affect the chemical equilibrium. The concept of "*active sites*" is often used to describe the surface atomic spot contributing the most towards the adsorption of intermediates during the electrochemical water splitting process. However, the mechanism of both the HER and OER depends on the acidity of the electrolyte, which might consist of multiple steps also involving a water dissociation. In this case, the active site will be a combination of several surface centers, not only one, with different adsorption properties to facilitate the optimum rate of all involved steps, including water surface dissociation. Therefore, to further address the activity of electrocatalysts in different media, this review will focus on a combination of several factors affecting the HER and OER processes for metal chalcogenides and phosphochalcogenides rather than looking for a true active site/sites of these materials. Namely, the role of electric conductivity (metallicity), adsorption kinetics of both hydrogen and oxygen intermediates, bifunctionally of the surface and surface functional groups (P, S or Se-based groups) on the electrochemical water splitting will be further discussed in this review.

### Electrical conductivity and metallicity

The electric conductivity of the catalyst has a strong influence on its overall electrocatalytic activity; however, the electric conductivity may be relevant for the dry materials as some changes in the surface chemistry are expected after the contact with the electrolyte. The changes in oxidation state and presence of surface functional groups can significantly affect the charge transfer process; therefore, the effective conductivity as the HER and OER descriptor should be measured only for activated catalysts directly from the solution.[58] The electrical conductivity might have an impact on the surface wettability of the electrocatalyst, which has to be investigated. In Fig. 2a, Mattia *et al.* showed that the contact angle between the carbon substrate and polar water or non-polar solvents depends on the annealing temperature of the pre-treated carbon material; however, in these conditions, it is difficult to separate the contribution of surface functional groups and electrical conductivity of the material.[59] Usually, the material with higher bulk electrical conductivity is more electrocatalytically active compared to the low electric conductive system (Fig. 2b); however, the surface reactivity towards adsorption/desorption of intermediates should be considered as well.[25,31,60–64]

### Hydrogen adsorption

The binding strength of adsorbed hydrogen on the active site of the catalyst is an important descriptor of the electrocatalytic HER activity of the material in acid media (Fig. 2). The catalyst with a strong binding strength of adsorbed hydrogen intermediates limits the desorption step (Tafel/Heyrovsky step), while the weak binding leads to poor adsorption-activation behaviour (Volmer step) according to the Sabatier principle (Fig. 2d). As shown in Fig. 2b, materials with a more metallic character often form stronger bonding with hydrogen compared to semiconductors upon adsorption of a proton. However, this binding strength of hydrogen intermediates (H*) does not solemnly depend on the electrical conductivity of the electrocatalyst, but is also influenced by its position in the conduction band and the Fermi level at the solid–liquid interface. The localized density of state measurement is an important way to understand the excess and/or deficiency of electrons at the specific surface centres,[65,66] which can be an indicator of the adsorption strength of the intermediates. Apart from that, the nature of the surface termination of the catalyst should be also considered due to the difference in electrocatalytic activity of exposed adsorption sites.[67,68] Specifically, the HER occurring predominantly through the chalcogenide site makes $NiS_2$ more active compared to $NiSe_2$, whereas the opposite trend can be observed for the HER occurring on the metal site.[69,70] It was shown that the position of the conduction band of the active site located above the standard hydrogen electrode (SHE) leads to weak bonding with adsorbed hydrogen, while a conduction band lower than SHE shows the

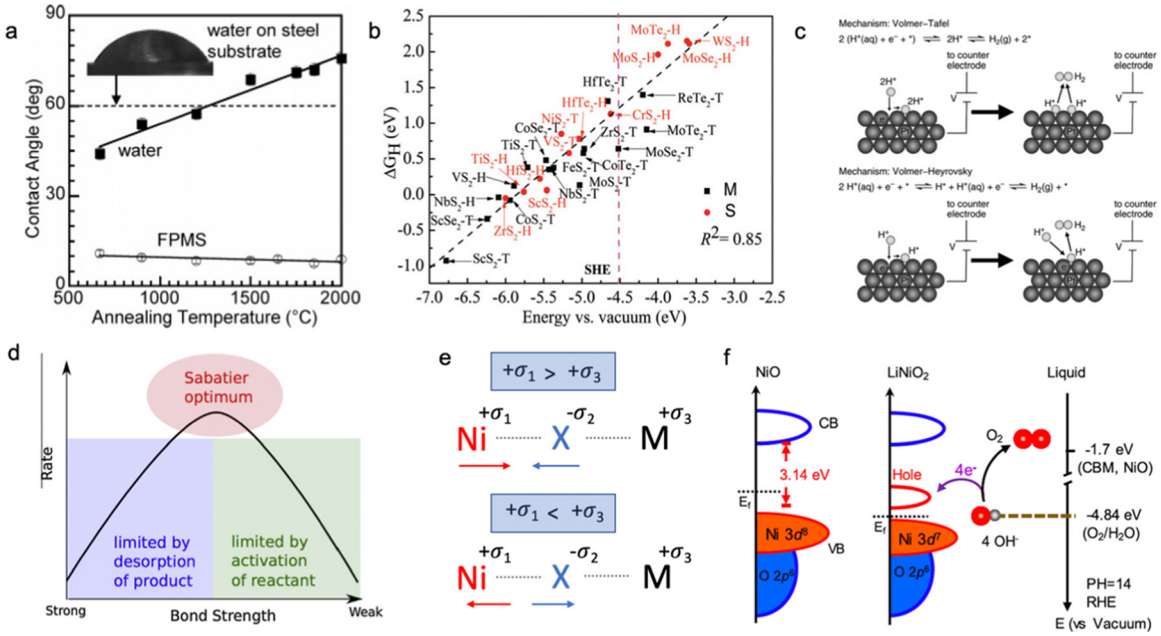


Fig. 2 (a) Contact angle on CVD-carbon film deposited on glassy carbon: contact angle for water and nonpolar fluorosilicone (FPMS) as a function of annealing temperature and electrical conductivity of the carbon substrate. Reproduced with permission from ref. 59. Copyright © 2006, American Chemical Society. (b) The hydrogen adsorption free energy $\Delta G_H$ as a function of the conduction band minimum $E_{cv}$ for a 2 × 2 supercell of transition metal dichalcogenides. The pink dashed lines indicate the SHE, and S and M indicate semiconductor and metallic, respectively. Reproduced with permission from ref. 60. Copyright © 2017, the Royal Society of Chemistry. (c) Volmer–Tafel and Volmer–Heyrovsky hydrogen evolution reaction mechanism in acid and alkaline media. Reproduced with permission from ref. 79. Copyright © 2012, American Chemical Society. (d) Sabatier principal volcano plot for the binding energy of adsorbed intermediates. Reproduced with permission from ref. 80. Copyright 2015 Elsevier Ltd. (e) Schematic illustration of chemical bond hybridization between chalcogen (X) and nickel (Ni) atoms upon doping of metal (M). (f) Schematic diagram for electronic structures of NiO and $LiNiO_2$ (left) and energy diagram at the oxide–liquid interface on the vacuum level scale at pH = 14 (right); the redox level for $O_2/H_2O$ (red dashed line) is −4.84 eV, the conduction band minimum (CBM) level for NiO is −1.7 eV according to the formula: $E_{CBM} = E_{bandgap} - E_{ionization}$, ($E_{bandgap}$ = 3.7 eV, $E_{ionization}$ = 5.4 eV). Reproduced with permission from ref. 78. Copyright © 2019, American Chemical Society.

opposite trend with strong adsorbed H* intermediates.[60] This is also related to the occupancy of the conduction band and type of semiconductor; the very high occupancy of the conduction band is unfavourable for the acceptance of one extra electron from the hydrogen, and subsequently, this leads to weak bonding (anti-bonding).

Therefore, the electrocatalyst should have a partially occupied and low-energy conduction band for stronger hydrogen bonding; and modification of the material between n-type and p-type semiconductors might be an effective strategy.[71–74]

### Oxygen intermediate adsorption

Speaking of the oxygen evolution reaction, this process is controlled by the binding strength of oxygen-based intermediates (O*, OH*, OOH*), and the ideally performing water oxidation electrocatalyst binds these species neither too strongly nor too weakly.[61,63] Previously, it was mentioned that the space charge layer at the surface of the electrode affects the resulting potential drop of the Helmholtz layer along with the energy barrier for the charge transfer kinetics, and, therefore, it directly influences the concentration of hydroxyl anions and adsorption strength of oxygen-containing intermediates.[63] In this regard, it is believed that p-type semiconductors are more suitable catalysts for the OER compared to n-type ones, as p-type semiconductive materials possess more positive near-surface potential with large availability of holes on the electrode surface for stabilization of adsorbed oxygen-based intermediates.[75,76] As shown in Fig. 2e, metal doping has a profound impact on the hybridization state of the metal–chalcogenide bond; namely, for doping metals in an oxidation state less positive than that of nickel, nickel shares more electrons with the chalcogenide making the metal–chalcogenide bond shorter and the chalcogenide more negative. Meanwhile, doping Ni–X with highly positive M leads to an opposite effect, namely, the metal–chalcogenide bond gets longer with higher electron occupancy on the Ni site. According to the theory of charge transfer,[77] electron transfer can take place only from any occupied state to an unoccupied state if their energies are matched. For reduction, the electrons transfer from the occupied state of the electrode to the unoccupied state of the electroreactant, while for oxidation the receiving state will be on the electrode. The strong overlap of the occupied and unoccupied states near the Fermi level on the electrocatalytic electrode will minimize the overpotential needed for charge transfer. Suntivich *et al.* have shown this for perovskite oxides and another work has been done for the $Li_xNi_{1-x}O$ catalyst, which shows higher electrocatalytic activity towards the OER upon Li doping due to hybridization of the Ni–O bond and the

creation of more vacancies for electron acceptance upon adsorption of oxygen-based intermediates, as shown in Fig. 2f, where a new unoccupied state emerges near the Fermi level.[61,78]

### Bifunctionality of the surface

As mentioned above, the acidity of the electrolyte has a strong influence on the electrocatalyst rate performance, and hydrogen evolution in neutral/alkaline media requires an overpotential associated with a decrease in a number of electroactive species, namely $H^+$, according to the Nernst equation.[81] So, an extra step such as "water dissociation" takes place to generate electroactive species for both cathodic and anodic reactions. In this regard, the proper combination of surface neighbours, *i.e.*, active sites, for facile water deprotonation, recombination of intermediates, and gas desorption can improve the efficiency of the HER rate even at high pH values and/or improve the OER in acidic media.[22,51,82–84] This phenomenon is called "*bifunctionality*", namely, the catalyst should possess both strong and weak bonding active sites responsible for the adsorption of O*-based intermediates and recombination/desorption of H* intermediates (Fig. 3). This can be achieved by TM doping with different oxophilicity; for example, the Ni–Pt(111) surface shows lower HER overpotential in alkaline media than that of non-doped Pt(111).[85] In this case, the hydrophilicity of Pt(111) improves with Ni doping and more protons can be electrogenerated upon adsorption of water molecules. A similar observation was done for TM doping in the $NiPS_3$ phase, where a proper combination of TM with different oxophilicity and doping ratio leads to more active HER and OER behaviour.[32,86] Also, highly oxophilic vanadium was successfully used in the $Co_{1-x}V_xPS$ electrocatalyst to accelerate the water dissociation kinetics.[87] Thus, both the H* and O* intermediate bonding strength should be taken into account to comprehensively evaluate the impact of the electrocatalyst nature on the water splitting mechanism.[82]

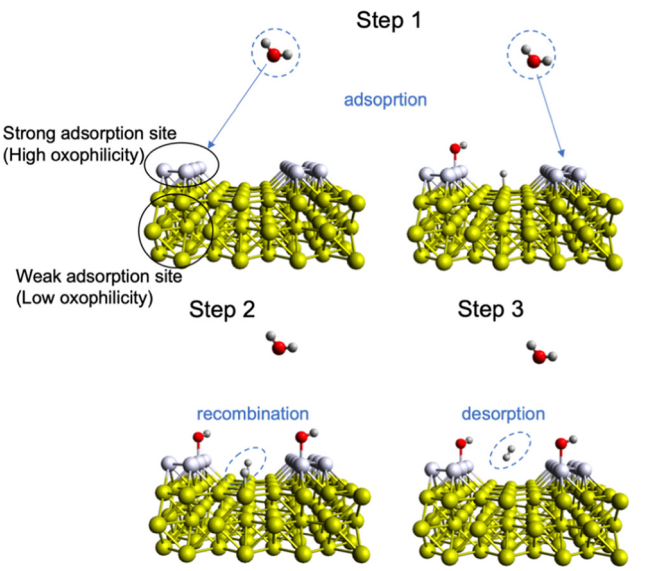


Fig. 3 Mechanism of surface bifunctionality for the Volmer–Tafel HER reaction in neutral/basic media where water dissociation takes place.

### Surface functional groups (P, S or Se-based groups)

Anion nature and its chemical response to changes in the acidity of the electrolyte can significantly affect the reactivity of the electrocatalyst. It was shown that the MoP(001) surface shows high activity towards the HER in neutral media, where Mo sites help to adsorb water and MoP sites recombine H* into $H_2$.[88] Meanwhile, an excess of $H^+$ or $OH^-$ alternates the surface and block sites for the dissociation of water, which leads to poor electrocatalytic behaviour. Fang *et al.* show that P-doping improves the H* desorption/recombination process in bimetallic NiCo alloy, while Se and O-doping show the opposite trend.[89] This is due to the difference in electronegativity of the anion, which follows the trend O (3.44) > Se (2.55) > P (2.19), and both O and Se demonstrate very strong hydrogen adsorption enthalpies. Li *et al.* showed that incorporating Se-vacancies into $Ni_2P$ ($Ni_2P/Ni_3Se_4$) significantly improves the HER activity due to an increase in adsorption energy for the H* intermediate on the Se site.[90] In the case of bimetallic nickel–iron oxide, the introduction of sulphur to oxygen vacancies also showed surface charge delocalization to iron sites, *i.e.*, more electrons on iron sites after sulphur doping, which is again due to the difference in the electronegativity of the anions (S (2.58) *vs.* O (3.44)).[65] Such changes in surface charge between neighbours contribute a significant role to the bifunctionality of the electrocatalyst as well as its electronic conductivity (band gap value).

Regarding the effect of anion chemistry on the OER behaviour, Wu *et al.* show that $S^{2-}$-vacancies in NiFe are responsible for high water oxidation activity, which changes to $SO_x$ form after long-term cycling. This process was attributed to surface poisoning and deterioration of the OER activity of the electrocatalyst. However, Hu *et al.* showed that the chalcogenide anion of $CuO@CuS_x$ leaches into the electrolyte during cycling and $SO_4^{2-}$ is formed.[91] The presence of $SO_4^{2-}$ in the solution and the oxidized CuO@CuOOH surface leads to an interfacial abundance of $OH^-$ which improves the OER activity. The leaching of chalcogenide anions during the OER was seen in many literature reports.[92–95] However, some reports focus unjustifiably too much on the structure of the pre-catalyst to describe the OER mechanism rather than comprehensively investigating the activated surface of the electrocatalyst.[96] As for phosphide and phosphate anions, the electrocatalysts with these compounds also demonstrated an improved behaviour for water oxidation;[97,98] however, again more studies are needed to understand the difference between pre-catalyst and real active sites.

## Metal-doped nickel phosphochalcogenides ($NiPX_3$)

$MPS_3$ (M = Cu, Ni, Fe, Co, Mn) are semiconductors with a band gap in the range of 1.3–3.5 eV, whereas $MPSe_3$ (M = Cu, Ni,

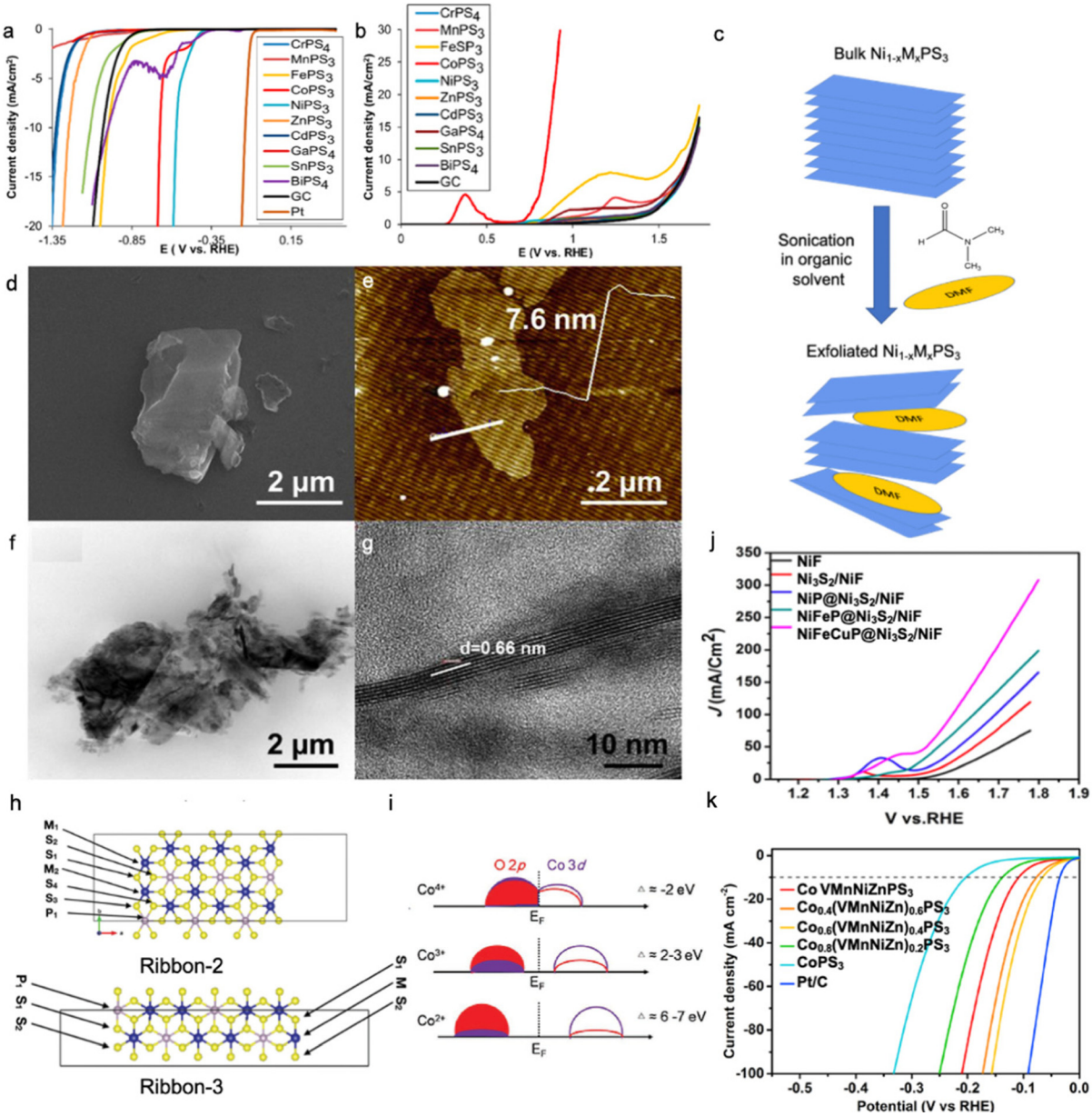


Fig. 4 LSV curves for (a) HER and (b) OER activity of bulk $MPS_3$ phases. Reproduced with permission from ref. 31. Copyright © 2017, American Chemical Society. (c) Schematic illustration of $Ni_{1-x}M_xPS_3$ (where M is a doping metal) nanosheet preparation by exfoliation of bulk crystals in organic solvent (*N,N*-dimethylformamide (DMF)). Images of Mn-doped $NiPS_3$ nanosheets prepared by the synthetic route in Fig. 3c were obtained by (d) SEM, (e) AFM, and (f and g) TEM. Reproduced with permission from ref. 22. Copyright 2018 Elsevier Ltd. (h) Possible edges of the $MPS_3$ material with adsorption sites. Reproduced with permission from ref. 122. Copyright © 2021, the Royal Society of Chemistry. (i) Charge transfer model of $Co^{2+}$, $Co^{3+}$, $Co^{4+}$ in a covalent system. Reproduced with permission from ref. 123. Copyright 2021, Wiley-VCH. (j) LSV curves for the OER activity of trimetallic phosphides grown on $Ni_3S_2$/Ni foam. Reproduced with permission from ref. 140. Copyright © 2020, American Chemical Society. (k) LSV curves for the HER activity of high entropy $CoPS_3$-based alloy. Reproduced with permission from ref. 121. Copyright © 2022, American Chemical Society. All reported polarization curves were recorded in 1.0 M KOH.

Fe, Co, Mn) show more metallic behaviour[29,64,99] and the conduction band is mainly formed by $[P_2S_6]^{4-}$ or $[P_2Se_6]^{4-}$ frameworks where the metal contributes to the occupancy of the states.[100] In general, $MPSe_3$ phases outperform $MPS_3$ phases in electrocatalytic activity due to higher electrical conductivity leading to better charge transfer kinetics,[32,36,64,101,102] where the $M_xP_y$ phase is found to be more electrocatalytically active than the $M_xS_y/M_xSe_y$ phase for both HER and OER processes.[103–105] As shown in Fig. 4a and b, electrocatalytic hydrogen evolution was studied for $MPS_3$ bulk phases, and the lowest overpotential was found for $NiPS_3$; meanwhile, $CoPS_3$ shows superior OER performance to other $MPS_3$ materials.[31] As said above, the HER activity greatly depends on the adsorption strength of H* intermediates to the catalyst surface, and a

rational combination of both weak and strong adsorption centres can be an effective strategy to optimize the electrocatalyst performance.

Song *et al.* showed that $NiPS_3$ possesses both weak and strong H* adsorption centres, whereas $FePS_3$ has only weak H* centres with $\Delta G_H > 0$ eV.[32] The electronic structure analysis shows that the lowest unoccupied molecular orbital (LUMO) at the conduction band, which is responsible for the electron acceptance, is located at a different position for $MPS_3$ (M = Ni, Fe, Mn).[106] Specifically, the LUMO of $NiPS_3$ represented by the $e_g$ orbital is at relatively higher energy than $t_{2g}$ of $FePS_3$ and $MnPS_3$, therefore showing that $NiPS_3$ will be in favour of the Tafel/Heyrovsky desorption step compared to other $MPS_3$ phases due to weaker electron affinity.[31] The excellent water oxidative activity of $CoPS_3$ is the most likely due to higher $Co_xP_y$ activity compared to the $Ni_xP_y$ phase.[107–109] The band gap of $NiPS_3$ was found to be 1.4–1.8 eV experimentally,[110,111] while density functional theory gives a wider range of values 1.0–2.19 eV resulting from the choice of the basis set, temperature effect and zero-point motion correction term.[43,110,112] The valence band of $NiPS_3$ consists of up-spin 3d $e_g$ of nickel, 3s of phosphorous, and 3p of sulphur, whereas the conduction band is dominated by down-spin 3d $e_g$ of nickel.[113] The position of the metal d-band near the Fermi level means that the nickel centre will likely accept an electron during the cathodic reaction.

Metal-doped $NiPS_3$ phase can be synthesized *via* different methods such as solid-state synthesis,[22] solvothermal,[114] and chemical vapour deposition;[43,115] however, precise control of stoichiometry can be better realized only through solid-state synthesis in an inert atmosphere. In this method, elemental powders are mixed in their stoichiometric ratio and annealed at high temperatures in a degassed quartz tube. To further expose the active surface area, the as-synthesized bulk phase can be sonicated in an organic solvent to allow exfoliation across a van der Waals gap (Fig. 4c), where the degree of exfoliation can be controlled by the nature of the organic solvent and sonication conditions.[116,117] Fig. 4d–g show the morphology of Mn-doped $NiPS_3$ nanosheets prepared by solid-state synthesis and exfoliation with *N,N*-dimethylformamide (DMF). Table 3 shows the summary of some synthesis methods for metal phosphochalcogenides.

Alam *et al.* investigate the nature of the active sites in $CoPS_3$ and $NiPS_3$ monolayer sheets, which demonstrated the highest activity on the edges compared to that on the plane, similar to the $MoS_2$ phase.[122] Detailed analysis of the hydrogen adsorption free energy on each atom of the investigated edge ribbons (Fig. 4h) shows that during both the first and second hydrogen adsorption steps, $CoPS_3$ shows stronger adsorption on both metallic and sulphur/phosphorous sites compared to that of $NiPS_3$. Metallic adsorption sites of $NiPS_3$ show a positive free energy value unlike that for $CoPS_3$, whereas sulphur and phosphorus always interact strongly with adsorbed hydrogen for these two phases. These differences in adsorption sites indicate why the HER for $CoPS_3$ occurs *via* the Volmer–Tafel step with high coverage of adsorbed hydrogen, while that in $NiPS_3$ happens through Volmer–Heyrovsky with low coverage of adsorbed hydrogen.

Considering the difference in electrocatalytic activity of $NiPS_3$ and $CoPS_3$ and their difference in the adsorption strength of hydrogen, it is important to ask why $NiPS_3$ outperforms $CoPS_3$ in the HER but underperforms that in the OER. This is related to the formation of high valence metallic states such as $Co^{3+}/Co^{4+}$ during the water oxidation, which strongly

Table 3 Synthesis details of selected metal phosphochalcogenides

| Material | Metal precursors | Source of P/S | Method of synthesis | Ref. |
|---|---|---|---|---|
| Bulk $MPS_3$ (M = Ni, Co, Fe, Mn) | Metal powders | Phosphorous, sulfur | Sealed under high vacuum and annealed in a quartz glass ampule at 650/750 °C for 120/288 h | 31 |
| Bulk $MPSe_3$ (M = Ni, Co, Fe, Mn) | Metal powders | Phosphorous, selenium | Sealed under high vacuum and annealed in a quartz glass ampule at 650 °C for 240 h | 45 |
| Exfoliated $MnPX_3$ (X = S, Se) | Metal powders | Phosphorous, sulfur | Similar to ref. 31, then sonicated in sodium cholate at 750 W for 1 h and collected after centrifugation | 36 |
| Exfoliated $FePSe_3$ | Metal powders | Phosphorous, sulfur | Similar to ref. 31, then sonicated in acetone–water mixture for 4 h and collected after centrifugation | 36 |
| Exfoliated $NiPS_3$ | Metal powders | Phosphorous, sulfur | Similar to ref. 31, then sonicated in CTAB mixture for 10 h and collected after centrifugation | 118 |
| $NiPS_3$/C or $CoNiPS_3$/C | Ni–Co Prussian blue analogue | Phosphorous, sulfur | Prepared Ni–Co PBA placed in a tube furnace for annealing. Synthesised samples were washed with $CS_2$ and $HCCl_3$ | 43 |
| Bulk $Cu_2P_2S_6$ | $Cu_2S$ | $P_2S_5$ | Stoichiometric mixture was vacuum sealed in a quartz tube and annealed at 623 K for 24 h | 119 |
| $Cu_3PS_4$ | Cu powder | Phosphorous, sulfur | Stoichiometric mixture was vacuum sealed in a quartz tube and annealed at 800 K for one week | 120 |
| $Ni_{0.7}Fe_{0.3}PS_3$/Mxene | $Ni(NO_3)_2{\cdot}6H_2O$ ($\geq$98.5%), $Fe(NO_3)_3{\cdot}9H_2O$ ($\geq$98%) | Phosphorous, sulfur | Transitional metal layered hydroxide aqueous solution was mixed with $Ti_3C_2T_x$ solution, and the mixture was ultra-sonicated for 1 h. The as-obtained nanocomposites were preheated in an Ar atmosphere at 300 °C for 1 h, then mixed with red phosphorus and sulphur powder in a molar ratio of 1 : 3 and vacuum sealed in a quartz tube for annealing | 44 |
| Metal doped $NiPS_3$ | Metal powders | Phosphorous, sulfur | Sealed under high vacuum and annealed in a quartz glass ampule at 650/750 °C for 120/288 h | 22, 32, 86 and 121 |

absorbs $H_2O$ and $OH^-$ as well as a higher degree of covalency between the metal and oxygen, which decreases the value of the charge transfer due to the hybridization of 3d and 2p orbitals (Fig. 4i).[123]

The Xu group studied the Co-doped $NiPS_3$ phase towards hydrogen evolution activity, and $Ni_{0.95}Co_{0.05}PS_3$ nanosheets appeared to be the catalyst with an optimal composition having an overpotential of 71 mV *vs.* RHE at −10 mA $cm^{-2}$ and Tafel slope of 77 mV $dec^{-1}$ at 1.0 M KOH,[86] and the Co-doped sample was found to be more electrically conductive than the $NiPS_3$ phase by three orders of magnitude. This agrees with a decreased value of band gap that was previously seen for Co-doped nickel sulphides from ∼1.4/1.2 eV to 0.17/0.08 eV.[124] The nickel phosphides show a metallic nature with a metal d-band located near the Fermi level[125,126] with phosphorous 3s and 3p states located mostly in the conduction band much lower than the Fermi level. The Co-doping to nickel phosphide phase shifts the nickel 3d band to the Fermi level, which creates a hole state, optimizing the value of free energy for hydrogen adsorption compared to other undoped Co/Ni.[127,128] This also corresponds to the lower band gap for the Co-doped $NiPS_3$ phase, *e.g.*, 1.47 eV for $CoNiPS_3$ *vs.* 1.50 eV for $NiPS_3$ eV, which demonstrates excellent HER/OER activity on the N-doped carbon substrate compared to non-doped pure $NiPS_3$ phase.[43]

Fe-doped $NiPS_3$ phase has been widely studied for electrochemical water splitting, and the $Ni_{0.9}Fe_{0.1}PS_3$ phase demonstrated excellent HER (72 mV *vs.* RHE at −10 mA $cm^{-2}$ and Tafel slope of 73 mV $dec^{-1}$) and OER (329 mV *vs.* RHE at 20 mA $cm^{-2}$ and Tafel slope of 69 mV $dec^{-1}$) in 1 M KOH.[32] The same composition demonstrated good HER activity of 196 mV@10 mA $cm^{-2}$ on MXene nanosheets, while the OER activity was optimized with a relatively larger Fe content of $Ni_{0.7}Fe_{0.3}PS_3$@MXene (282 mV@10 mA $cm^{-2}$).[44] For the HER, it was shown that Fe-doping narrows the band gap of the material, which leads to better charge transfer as well as optimizes the H* binding energy ($\Delta G_H$ ∼ 0.00 eV).[32,129] Meanwhile, the enhancement in the OER activity upon Fe-doping is most likely due to the formation of highly active Ni(Fe)OOH species.[32,44,130] The catalyst surface undergoes severe oxidation within an anodic scan, and the metal oxide phase will contribute a major part to the OER performance of the catalyst due to reduced charge trasnfer resistance.[118]

R. Subbaraman *et al.* showed that the OH–$M^{2+\delta}$ bond is a fundamental descriptor of the HER/OER activity of metal oxide-based electrocatalysts, and this bond strength increases in the following trend Mn > Fe > Co > Ni, which corresponds to a decrease in catalyst reactivity, namely, the reactivity falls in accordance with Ni > Co > Fe > Mn.[131] Despite successful $NiPS_3$ doping by Co and Fe, the HER activity was not improved upon Mn doping,[22] which might be related to the large band gap of $MnPS_3$ and relatively strong $H_2O$ adsorption due to the low position of the LUMO within the conduction band.[29,106,132] Apart from that, the MnP phase does not show any active sites with ideal $\Delta G_H$ (within ±0.2 eV) compared to those of NiP, CoP and FeP analogues.[133] The corresponding decrease in OER activity of $NiPS_3$ upon Mn doping is in good agreement with the formation of $MnO_2$ which strengthens the OH–$M^{2+\delta}$ bond and hinders the Tafel/Heyrovsky recombination–desorption step. Besides, the Mn doping also increases the level of metal–oxygen covalency due to 3d and 2p hybridization (Ni–O is 2.09 Å *vs.* Mn–O is 1.92 Å), namely, the 2p hole state near the Fermi level disappears with an increase of Mn content, which leads to stronger interactions with adsorbed intermediates.[134] The stronger adsorption character and lower electrical conductivity correlate with increased electron affinity for the $Mn^{4+}$ state affecting the charge transport.[135] This is also evidenced by the increasing dominance of the Volmer step for both HER and OER processes with Mn-doped $NiPS_3$.[22] In this sense, the $NiPS_3$ doping with low oxophilic metals, such as Cu, should be considered to further expand the role of oxophilicity on the performance of the $NiPS_3$ electrocatalyst,[119,136] especially knowing that a successful synergetic effect can be achieved in their mixed phosphides.[136] Also, Cu doping in the NiS@$Ni_2P$ phase demonstrated a positive effect on the electrocatalytic HER activity of the nickel-foam-based catalyst.[137] The 10 weight % Cu doping in $NiPS_3$ showed a stable photocathodic HER behaviour in 0.5 M $H_2SO_4$,[138] and the electronic structure of this doped phosphochalcogenide is a p-type semiconductor, which might be beneficial for the electrochemical OER as mentioned above. Cu alloying with sulphur and phosphorus sources can give $Cu_3PS_4$ and $Cu_2P_2S_6$ phases,[119] and the DFT calculation for the $CuPS_3$ monolayer revealed its small band gap of 1.63 eV.[139] Although, $CuPS_3$ has never been reported for electrochemical water splitting, it will likely be less active than pristine $NiPS_3$; however, the presence of Ni in the $CuPS_3$ phase can give a very low value for hydrogen adsorption energy, *e.g.*, 0.09 eV similar to that of Pt surfaces of −0.09 eV.[139] Therefore, it will be interesting to see some work on the synthesis and application of the Cu-doped $NiPS_3$ phase towards the HER and OER.

Last but not least, it might be also useful to consider three or more metal-based $MPX_3$ phases for electrochemical water splitting (Fig. 4j and k) to properly adjust the surface bifunctionality and electronic properties.[121,140,141] The electrocatalytic activities of selected metal phosphochalcogenides towards the HER and OER are summarised in Tables 4 and 5.

## Metal doped nickel chalcogenides ($Ni_aX_b$, X = S, Se)

Nickel chalcogenides, such as sulphides and selenides, are found in different stoichiometric and non-stoichiometric compositions, namely, NiX, $NiX_2$, $Ni_3X_2$, and $Ni_9X_8$. Both sulphides and selenides are insoluble in water and stable within neutral and near-neutral pH; also, their surfaces are covered with oxide/hydroxide films under harsh alkaline conditions, making them highly suitable for HER electrocatalysts and OER precatalysts.[26] However, these compounds are highly unstable within acidic conditions due to the dissolution of chalcogenides.[26] It was found that the HER electrocatalytic activity of nickel selenides changes in the following order $Ni_3S_2$ > $NiS_2$ > NiS, which was attributed to the higher electrical conductivity of $Ni_3S_2$.[144]

Table 4 HER properties of selected metal phosphochalcogenides in different aqueous media. All catalysts were studied with a glassy carbon electrode substrate unless mentioned differently, *e.g.*, carbon cloth.[a] The nanosheet morphology was denoted as NSs

| Materials | Loading mass, μg $cm^{-2}$ | $j@\eta$, mA $cm^{-2}$@mV | Electrolyte | Ref. |
|---|---|---|---|---|
| NSs $NiPS_3$ (thickness = 4 nm) | 510 ± 10 | 10@193 | 1.0 M KOH | 32 |
| NSs $CoPS_3$ (thickness = 2.8 ± 0.7 nm) | 350.0[a] | 10@202.8 | 1.0 M KOH | 121 |
| NSs $FePS_3$ (thickness = 0.7 to 1.7 nm) | 150 | 10@337 | 0.5 M KOH | 142 |
| NSs $FePSe_3$ (thickness = 0.7 to 1.7 nm) | 150 | 10@309 ± 2 | 0.5 M KOH | 101 |
| NSs $FePSe_3$ (thickness = 0.7 to 1.7 nm) | 150 | 10@195 ± 3 | 0.5 M $H_2SO_4$ | 101 |
| NSs $MnPS_3$ (thickness = 38.1 ± 11.2 nm) | 141.5 | 10@1090 ± 71 | 1.0 M KOH | 36 |
| NSs $MnPS_3$ (thickness = 38.1 ± 11.2 nm) | 141.5 | 10@835 ± 68 | 0.5 M $H_2SO_4$ | 36 |
| NSs $MnPSe_3$ (thickness = 16.7 ± 9.3 nm) | 141.5 | 10@992 ± 56 | 1.0 M KOH | 36 |
| NSs $MnPSe_3$ (thickness = 16.7 ± 9.3 nm) | 141.5 | 10@640 ± 87 | 0.5 M $H_2SO_4$ | 36 |
| NSs $MnPS_3$ (thickness = 7.6 nm) | 1250 | 10@1140 | 1.0 M KOH | 22 |
| NSs Co-doped $NiPS_3$ (0% Co doping) (thickness = 6.7 nm) | 510 ± 10 | 10@∼220 | 1.0 M KOH | 86 |
| NSs Co-doped $NiPS_3$ (5% Co doping) (thickness = 6.7 nm) | 510 ± 10 | 10@71 | 1.0 M KOH | 86 |
| NSs Co-doped $NiPS_3$ (9% Co doping) (thickness = 6.7 nm) | 510 ± 10 | 10@145 | 1.0 M KOH | 86 |
| NSs Fe-doped $NiPS_3$ (0% Fe doping) (thickness = 4 nm) | 510 ± 10 | 10@193 | 1.0 M KOH | 32 |
| NSs Fe-doped $NiPS_3$ (5% Fe doping) (thickness = 4 nm) | 510 ± 10 | 10@130 | 1.0 M KOH | 32 |
| NSs Fe-doped $NiPS_3$ (10% Fe doping) (thickness = 4 nm) | 510 ± 10 | 10@72 | 1.0 M KOH | 32 |
| NSs Fe-doped $NiPS_3$ (15% Fe doping) (thickness = 4 nm) | 510 ± 10 | 10@152 | 1.0 M KOH | 32 |
| NSs Mn-doped $NiPS_3$ (0% Mn doping) (thickness = 7.6 nm) | 1250 | 10@320 | 1.0 M KOH | 22 |
| NSs Mn-doped $NiPS_3$ (5% Mn doping) (thickness = 7.6 nm) | 1250 | 10@380 | 1.0 M KOH | 22 |
| NSs $Co_{0.6}(VMnNiZn)_{0.4}PS_3$ (thickness 2.8 nm) | 350.0[a] | 10@65.9 | 1.0 M KOH | 121 |
| $NiPS_3$/C nanoshape | 300 | 10@∼330 | 1.0 M KOH | 43 |
| $CoNiPS_3$/C nanoshape | 300 | 10@∼140 | 1.0 M KOH | 43 |

Table 5 OER properties of selected metal phosphochalcogenides in aqueous media. All catalysts were studied with a glassy carbon electrode substrate. The nanosheet morphology was denoted as NSs

| Materials | Loading mass, μg $cm^{-2}$ | $j@\eta$, mA $cm^{-2}$@mV | Electrolyte | Ref. |
|---|---|---|---|---|
| NSs $NiPS_3$ (thickness = 0.64 nm) | 382 | 10@350 | 0.1 M KOH | 118 |
| NSs $CoPS_3$ | | 10@378 | 1.0 M KOH | 143 |
| $NiPS_3$/C nanoshape | 300 | 30@∼330 | 1.0 M KOH | 43 |
| $CoNiPS_3$/C nanoshape | | 30@∼285–250 | 1.0 M KOH | 43 |
| NSs rGO-$FePSe_3$ | 150 | 10@430 | 0.5 M KOH | 101 |
| $Ni_{0.7}Fe_{0.3}PS_3$@MXene | 250 | 10@282 | 1.0 M KOH | 44 |
| NSs Fe-doped $NiPS_3$ (0% Fe doping) (thickness = 4 nm) | 510 ± 10 | 20@437 | 1.0 M KOH | 32 |
| NSs Fe-doped $NiPS_3$ (5% Fe doping) (thickness = 4 nm) | 510 ± 10 | 20@359 | 1.0 M KOH | |
| NSs Fe-doped $NiPS_3$ (10% Fe doping) (thickness = 4 nm) | 510 ± 10 | 20@329 | 1.0 M KOH | |
| NSs Fe-doped $NiPS_3$ (15% Fe doping) (thickness = 4 nm) | 510 ± 10 | 20@356 | 1.0 M KOH | |
| NSs Mn-doped $NiPS_3$ (0% Mn doping) (thickness = 7.6 nm) | 1250 | 10@295 | 1.0 M KOH | 22 |
| NSs Mn-doped $NiPS_3$ (5% Mn doping) (thickness = 7.6 nm) | 1250 | 10@350 | 1.0 M KOH | |

Meanwhile, the opposite result showed that NiS outperforms the $Ni_3S_2$ catalyst,[145] which is probably related to different phases of NiS and $Ni_3S_2$ having different exposed adsorption sites. As for selenides, $NiSe_2$ was found to be superior to other nickel selenide phases for both the HER and OER in 1.0 KOH.[146,147] A more comprehensive review of nickel chalcogenides and their synthesis, including tellurides, as catalysts for electrochemical water splitting, can be found in the literature.[26,148] Synthesis methods of some metal chalcogenides are shown in Table 6.

Wang *et al.* estimated the hydrogen evolution activity for different metal dichalcogenides, and it was found that $CoX_2$ has the lowest absolute value of H* adsorption.[60] As shown in Fig. 5a and b, Kong *et al.* demonstrated that the HER activity in 0.5 M $H_2SO_4$ decreases in the order of $CoX_2$ > $NiX_2$ > $FeX_2$,[149] which is most likely due to a decrease in electrical conductivity in $CoX_2$ > $NiX_2$ > $FeX_2$ and partial occupation of the conduction band in $CoX_2$ and $NiX_2$.[155,156] A similar trend for the dichalcogenide phase was observed towards the OER process in 1.0 M KOH on different substrates.[151,157,158] Regarding monochalcogenides, NiX and CoX also exhibited superior HER and OER activity in an alkaline medium;[153,159,160] however, FeS has also demonstrated superior activity towards the OER process, which might be due to different surface area and roughness factors between the examined metal monosulfides.[150,161–163] However, it is important to accurately estimate the active surface area of the catalyst to provide a meaningful comparison of the effect of the chemical nature of metal chalcogenides on their electrocatalytic activity.[164,165] The HER activity of both $MnS_2$ and MnS is the lowest compared to other chalcogenides due to weak hydrogen bonding to the surface resulting from the smallest DOS occupation near the Fermi level,[153,166,167] and the same conclusion was done towards the OER activity of manganese sulphide, which is most likely due to the strong OH–$M^{2+\delta}$ bond (Fig. 5c).[131]

It was shown that Co-doping in $Ni_aX_b$ improves both the HER and OER performance, which is in good agreement with the optimized H* adsorption energy and higher electrical conductivity of $CoX_2$.[149,155,168–171] As shown in Fig. 5d and e,

Table 6 Synthesis details of selected metal chalcogenides

| Material | Metal precursors | Source of S/Se | Method | Ref. |
|---|---|---|---|---|
| $MX_2$ (M = Ni, Fe, Co, and X = S, Se) | A metal film by e-beam evaporation | Selenium/sulphur power | Selenium/sulphur power and metal precursor heated with Ar flow in a tube furnace | 149 and 150 |
| Fe–$NiS_2$/CF | $Ni(NO_3)_2{\cdot}6H_2O$ (0.3 mmol), $Fe(NO_3)_3{\cdot}9H_2O$ (0.1 mmol) | Sulphur powder | Layered metal hydroxides are grown on a carbon fibre. Then, sulphur power and metal precursor are heated with Ar flow in a tube furnace | 151 |
| $Fe_xNi_{1-x}Se_2$ nanoparticles | Nickel acetylacetonate and iron acetylacetonate | Selenium powder | A mixture of 0.1 mmol of $Ni(acac)_2$, 0.1 mmol of $Fe(acac)_2$ and 0.4 mmol of selenium powder was dissolved in the mixed solution of organic solvents. Then, solvothermal synthesis was performed in the autoclave. Particles were collected by centrifugation | 152 |
| MS (M = Ni, Co, Fe, Mn) | Metal hexacyanoferrate (MHCF) (M = Ni, Mn, Fe, Co) | $Na_2S$ | Electrodeposition of metal hexacyanoferrate on the surface of the GC electrode by applying potential from 0 V to 1 V for 20 cycles. Then, the same electrodeposition with 10 mM of $Na_2S$ solution | 153 |
| Metal doped NiX/NF (X = S, Se) | Metal salts, nickel foam | Thiourea, selenium powered | Solvothermal synthesis in an autoclave with/without the addition of a reducing agent | 92 and 154 |

surface wettability plays a crucial role in attenuating the HER/OER overpotential, which mitigates near-surface insulating bubble adhesion due to the formation of a very low contact angle at the electrolyte/surface interface.[172,173] This phenomenon is significantly influenced by surface oxophilicity, *e.g.*, the ability to connect with oxygen-based species either through adsorption or formation of hydrogen/ionic bonds, which helps to improve the kinetics of the adsorption step.[174] However, when comparing any electrocatalyst grown on a 3D substrate it is important to study the electrochemical activity normalized by active surface area, not just by geometric surface area, to avoid misleading observations.[164,165] The improved HER performance, resulting from the increase in oxophilic high valence states decreasing the activation energy barrier, was shown for various Fe-doped $Ni_aX_b$ as nanoparticles deposited on the electrode or a composite architecture grown on a conductive substrate.[175–179] The excellent OER performance of Fe-doped $Ni_aX_b$ was attributed to the formation of the Ni(Fe)OOH phase,

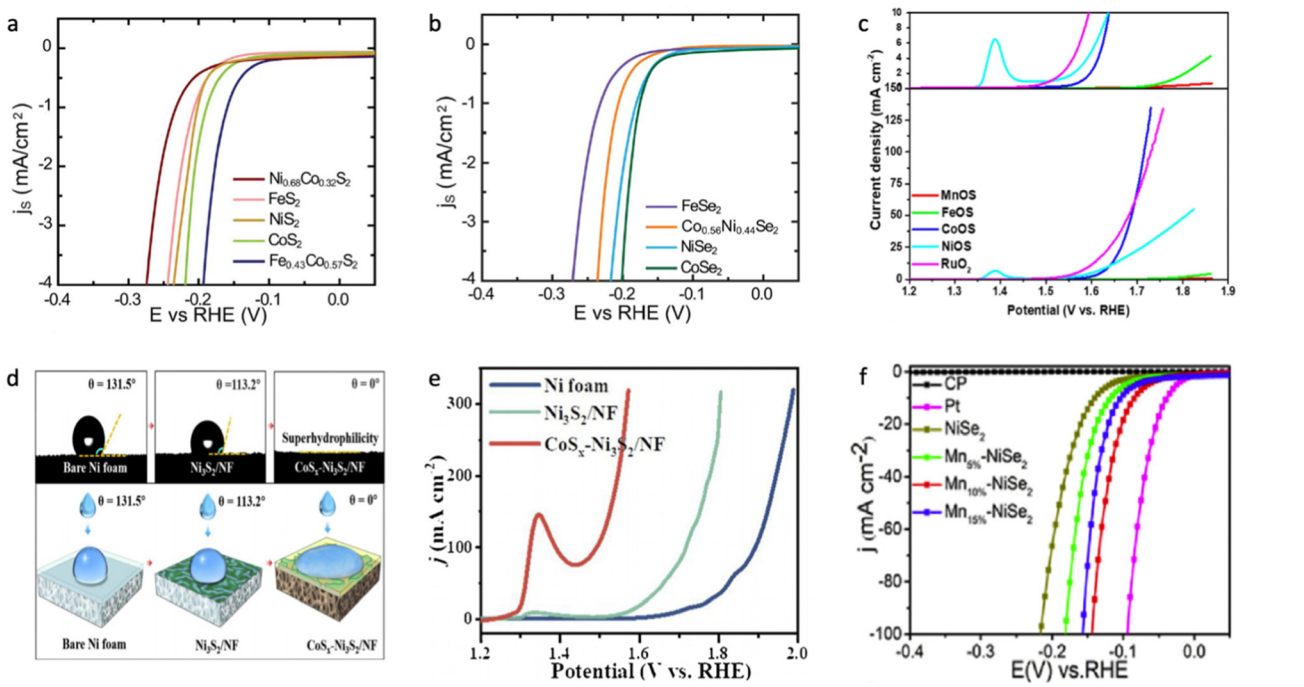


Fig. 5 (a) LVS curves of transition metal disulphides in which surface-area-normalized current density is plotted against the potential in 0.5 M $H_2SO_4$. (b) LVS curves of transition metal diselenides in which surface-area-normalized current density is plotted against the potential in 0.5 M $H_2SO_4$. Reproduced with permission from ref. 149. Copyright © 2013, the Royal Society of Chemistry. (c) LSV for sulphur-containing transition metal (hydro)oxides compared with commercial $RuO_2$ at 1.0 M KOH. Reproduced with permission from ref. 199. Copyright © 2020 Wiley Publications. (d) Contact angles of bare nickel foam (NF), $Ni_2S_3$/NF and $CoS_x$–$Ni_2S_3$/NF, where $CoS_x$–$Ni_2S_3$/NF shows superhydrophilic behaviour. (e) LVS for bare nickel foam (NF), $Ni_2S_3$/NF and $CoS_x$–$Ni_2S_3$/NF during the OER process in 1.0 M KOH. Reproduced with permission from ref. 172. Copyright 2020 Elsevier Ltd. (f) LSV curves of NiSe, Mn–NiSe, Pt/C and bare carbon fibre paper in 0.5 M $H_2SO_4$. Reproduced with permission from ref. 186. Copyright 2020 Elsevier Ltd.

which possesses high water oxidative activity due to the bifunctionality of the surface in the alkaline medium.[130,151,158,180–182] It was also shown that even the presence of 1.0 mM $Fe^{3+}$ impurities in alkaline electrolyte significantly increases the OER activity of the $NiO_xH_y$ phase.[183] This outstanding OER activity was attributed to the formation of a high oxidation Ni and Fe state, where Fe is an actual active site with an unoccupied state at the minimum of the conduction band.[183,184] In contrast to the poor HER/OER activity of Mn-doped $NiPS_3$, Mn-doped $Ni_aX_b$ materials show improved electrocatalytic behaviour compared to the non-doped sample (Fig. 5f),[185,186] and this is apparently due to the absence of electrocatalytically poor NiMnP and MnP phases.[187–189] It was shown that Mn doping in nickel sulphide leads to stronger $H_2O$ interaction energy and optimized H* adsorption energy on the catalyst surface, subsequently enhancing the HER performance in neutral and alkaline solution.[190] Although, the Mn doping in NiS leads to a large band gap from 2.05 eV for NiS to 2.31 eV for $Mn_{0.5}Ni_{0.5}S$, respectively.[124,191] It was also shown that Mn-doping in nickel-based oxides or chalcogenides shows a worse effect on the electrochemical water splitting performance than Co or Fe doping, which correlates with the poor conductivity and very strong oxophilicity of Mn-doped nickel-based catalysts.[192,193] It is likely that the successful Mn doping to nickel-based chalcogenides was just observed due to the overestimation of the active surface area of the electrocatalyst, especially for those samples prepared not through solid-state synthesis, although the positive effect of the oxophilic Mn states in nickel oxides or chalcogenides for the water dissociation step might take place. More investigation in this direction is needed to properly answer this question.

Yin *et al.* demonstrated that Cu, as well as Co, can improve the HER activity of NiS in 1.0 M KOH, which is due to changes in Ni electronic structure enabling the lower charge transfer resistance,[169] namely the doping makes the $e_g$–$t_{2g}$ gap (exited–transition state) for the 3d orbital small enough for fast charge transfer and increases the $Ni^{3+}$ content for a better adsorption mechanism. The CuNiS composite also demonstrated an outstanding OER activity in alkaline media with stronger $H_2O$ adsorption energy for Cu–NiOOH compared to the NiOOH phase.[194]

Wang *et al.* calculated $\Delta G_H$ for various metal-doped $NiSe_2$, and, in general, it was found that on both nickels, selenium, and the dopant site of (001), (110), and (111) plane Fe, Co, and Cu doping improves H* adsorption much better compared to other metals ($\Delta G_H \sim 0.0$ eV).[179] Besides, considering a trimetallic composition to optimize electrocatalyst performance again might be an effective strategy.[195–198] The electrocatalytic activities of selected metal chalcogenides towards the HER and OER are summarised in Tables 7 and 8.

Table 7 HER properties of selected metal chalcogenides in different aqueous media. The nanosheet morphology was denoted as NSs

| Materials | Loading mass, μg $cm^{-2}$ | $j@\eta$, mA $cm^{-2}$@mV | Electrolyte | Ref. |
|---|---|---|---|---|
| NiS | — | 10@169 | 1.0 M NaOH | 153 |
| CoS | — | 10@251 | 1.0 M NaOH | |
| FeS | — | 10@329 | 1.0 M NaOH | |
| MnS | — | 10@589 | 1.0 M NaOH | |
| NSs $NiS_2$ | — | 10@172 | 1.0 M KOH | 169 |
| NSs Co–$NiS_2$ | — | 10@80 | 1.0 M KOH | |
| NSs Fe–$NiS_2$ | — | 10@192 | 1.0 M KOH | |
| NSs Cu–$NiS_2$ | — | 10@143 | 1.0 M KOH | |
| NSs $NiS_2$ | 200 | 10@249 | 0.5 M $H_2SO_4$ | 175 |
| NSs Fe–$NiS_2$ | 200 | 10@121 | 0.5 M $H_2SO_4$ | |
| NSs $NiSe_2$/CF | 2000 | 10@207 | 1.0 M KOH | 186 |
| NSs Mn–$NiSe_2$/CF (10% Mn doping) | 2000 | 10@128 | 1.0 M KOH | |

Table 8 OER properties of selected metal chalcogenides in aqueous media. The nanosheet morphology was denoted as NSs

| Materials | Loading mass, μg $cm^{-2}$ | $j@\eta$, mA $cm^{-2}$@mV | Electrolyte | Ref. |
|---|---|---|---|---|
| NiOS/C | 240 | 10@420 | 1.0 M KOH | 199 |
| CoOS/C | 240 | 10@400 | 1.0 M KOH | |
| FeOS/C | 240 | 10@490 | 1.0 M KOH | |
| MnOS/C | 240 | 10@600 | 1.0 M KOH | |
| Fe–$NiS_2$/CF | 1410 | 20@243 | 1.0 M KOH | 151 |
| $NiSe_2$ | 450 | 10@305 | 1.0 M KOH | 152 |
| $FeSe_2$ | 450 | 10@332 | 1.0 M KOH | |
| $Ni_{0.25}Fe_{0.75}Se_2$ | 450 | 10@271 | 1.0 M KOH | |
| $Ni_{0.5}Fe_{0.5}Se_2$ | 450 | 10@235 | 1.0 M KOH | |
| $Ni_{0.75}Fe_{0.25}Se_2$ | 450 | 10@250 | 1.0 M KOH | |
| $Ni_2S_3$ | — | 100@450 | 1.0 M KOH | 200 |
| Co–$Ni_2S_3$ | — | 100@380 | 1.0 M KOH | |
| Fe–$Ni_2S_3$ | — | 100@270 | 1.0 M KOH | |
| Cu–$Ni_2S_3$ | — | 100@430 | 1.0 M KOH | |
| NiSe/NF | — | 50@420 | 1.0 M KOH | 201 |
| Co–NiSe/NF | — | 330@420 | 1.0 M KOH | |
| Cu–NiSe/NF | — | 380@420 | 1.0 M KOH | |

## Electrocatalytic stability

Several processes take place upon electrochemical water splitting, which directly affects the durability of the catalyst; for example, oxidation, elemental leaching, structural distortion and so on. Therefore, the rational design of electrocatalysts should consider the link between the electrocatalytic activity and the chemical stability of materials against degradation. Fig. 6 shows the relationships between electrocatalytic activity and chemical stability of transition metal dichalcogenides (TMDs) with different electronic structures.[25] The basal plane of TMDs with metallic character possesses higher electrocatalytic activity ($\Delta G_H \sim 0$ eV) than that of semiconducting materials ($\Delta G_H > 0$ eV), and the transition metal nature of metallic TMDs does not influence their activity much compared to that of semiconductors. Accordingly, metal doping for metallic TMDs might not be an effective strategy to optimize the performance of electrocatalysts, as it strongly influences the chemical stability of the material. As shown in Fig. 6b, most of the TMD edge sites are stable against the dissolution of chalcogens into the electrolyte ($\Delta G_{HX} < 0$ eV); therefore, the increase in the number of exposed edge sites of the catalyst is highly desirable to optimize the electrocatalytic activity. The chemical stability of electrocatalysts can be described according to their density of state in Fig. 6a, which shows that semiconductive materials with a higher occupancy in the valence band are more likely to transit electrons to the conduction band, which leads to higher activity

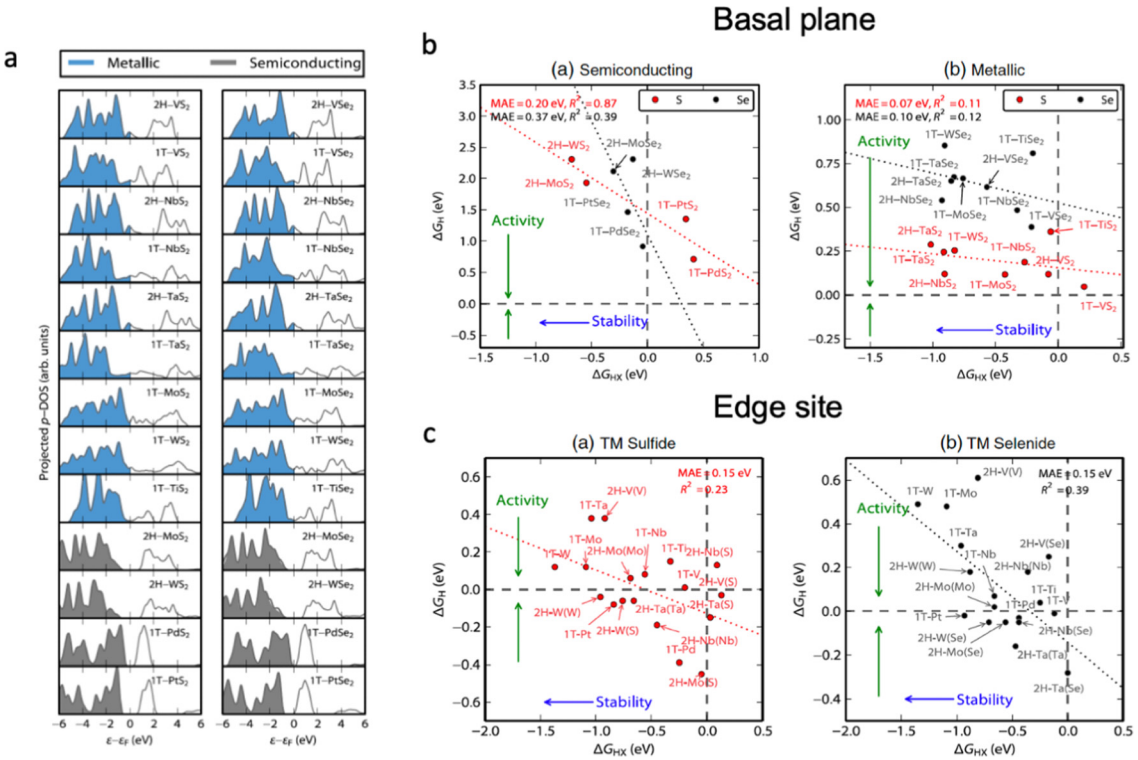


Fig. 6 (a) Projected density of states on the chalcogen atom (S or Se) for TMDs relative to the Fermi level, $E_f$. The blue densities of states indicate that the basal plane is metallic, whereas the grey ones are semiconducting. (b) Semiconducting single-layered TMD basal planes. The plot of the hydrogen adsorption free energy, $\Delta G_H$, as a function of the HX adsorption free energy, $\Delta G_{HX}$ (X = S or Se). (c) The differential hydrogen adsorption free energy $\Delta G_H$ as a function of the HX adsorption free energy at a corrosion resistance of $10^{-6}$ bar $H_2X$ (X = S or Se). The dashed lines indicate $\Delta G_H$ = 0 eV and $\Delta G_{HX}$ = 0 eV. The data span a narrow range of $\Delta G_H$ and the mean absolute errors are small, but the $R^2$ values are low due to the significant scatter. Reproduced with permission from ref. 25. Copyright 2015 Elsevier Ltd.

and lower chemical stability. For the metallic TMDs, the occupancy near the Fermi level as well as the vacancy of unoccupied orbitals plays the determining role in the catalyst stability. Additionally, the covalency of the metal–anion bond has to be taken into account to predict possible changes in oxidation states and phase transition during electrochemical water splitting; however, a compromise between the structural stability and high electrocatalytic activity of the material should be found.[134]

The mechanical damage caused by involving gas bubbles on the surface of the electrocatalyst is another problem, as the gas departure induces an opposite force towards the surface, which is proportional to the size of the bubble.[50,202,203] This might significantly influence the morphology of the electrocatalyst and its electrocatalytic stability; therefore, a super hydrophilic surface design with mechanically stable morphology, *e.g.*, preferably flat, should take place to facilitate gas detachment upon wetting of the nanopores. Other methods which can be utilized to enhance bubble detachment, such as the application of an external magnetic, ultrasonic fields, *etc.*, are thoughtfully discussed in the literature.[50]

## Summary and perspectives

Electrochemical water splitting has attracted enormous attention in recent years due to the rise of the fuel cell-based industry and global concern about climate change. Transition metal van der Waals materials, such as chalcogenides and phosphochalcogenides, have demonstrated a substantial electrocatalytic performance, which might be comparable with noble metal-based electrocatalysts upon surface defect engineering, high surface area morphology, and structure modification. Transition metal doping seems to be one of the best strategies to further enhance the performance of the host phase through overall electrical conductivity changes, bifunctionality of the surface, aerophobicity (hydrophilicity), *etc.*; however, this approach stills lacks a fundamental theory of "why and how" that can guide rational electrocatalyst design.

This review attempts to summarize recent advances in metal doping (Co, Fe, Mn, Cu) of nickel-based chalcogenides ($Ni_aX_b$, X = S and Se) and phosphochalcogenides ($NiPX_3$, X = S and Se) as a catalyst for electrochemical water splitting. This literature briefly introduced the main concepts of electrochemical water splitting as well as transition metal chalcogenides and phosphochalcogenides as a family of electrocatalysts. We explained the effect of anion nature on the electrocatalytic activity as well as its stability against leaching or oxidation. It is found that the relationship between electronic structure and electrocatalytic activity/stability for metal-doped nickel-based chalcogenides ($Ni_aX_b$, X = S and Se) and phosphochalcogenides ($NiPX_3$, X = S and Se) is not well conceptualized. The current practice to

improve the catalyst activity/stability possesses an arbitrary character that relies on empirical experience to optimize surface wettability, bifunctionality, electric conductivity, *etc.* Here, we show that doping of considered metals (Mn, Fe, Co, Cu) can improve the electrocatalytic behaviour of $Ni_aX_b$ either due to bifunctionality, *e.g.*, facile water dissociation step, and/or improving electrical conductivity except for Mn-doping, whereas doping in ($NiPX_3$, X = S and Se) shows more complex behaviour. Namely, the electrocatalytic activity of $NiPS_3$ is proportional to the activity of two different phases, *e.g.*, $Ni_xS_y$ and $Ni_xP_y$. The metal phosphide phase is more electrocatalytically active than the chalcogenide phase, and MnP is the least active phase amongst its counterparts, which results in Mn doping having a deteriorating impact on the HER/OER activity of ($NiPX_3$, X = S and Se) materials. Other considered doping metals (Co, Fe, Cu) except Mn unanimously demonstrated either success or promise for effective electrochemical water splitting with both chalcogenides and phosphochalcogenides. However, the doping ratio should be considered carefully to adjust the surface bifunctionality as well as the conductivity of the material. Mn doping for electrochemical water splitting should be considered very carefully over such doping as Cu, Co, and Fe in nickel (phospho)chalcogenides/oxides phases; this is due to a very high difference in the electron affinity and oxophilicity between Mn and Ni sites, which might lead to poor charge transport and dominant adsorption behavior during electrochemical water splitting.

This review explains the relationships between computational data for the electronic structure and experimental electrocatalytic changes in nickel-based chalcogenide and phosphochalcogenide electrocatalysts upon transition metal doping. Apart from the general suggestion to consider a larger variety of doping metals as well as to use more than one metal for doping to properly adjust the bifunctionality and electrical conductivity of the material, some gaps in the systematization of the current results should be considered for accurate comparison.

On the theoretical side, more systematic studies are needed to fulfil the gap between the correlation of electronic structure and electrocatalytic performance of transition metal-doped $Ni_aX_b$ and $NiPX_3$. When describing the free energy of the electrocatalyst during HER/OER processes, it is important to report the energy of the CB/VB regarding the vacuum reference to accurately compare it with SHE potential at the same scale. Electronic structure studies should consider a higher level of density functional theory than a local-density and generalized gradient approximation, such as Hubbard correction approaches, to accurately represent the density of states profile for semiconductive phases. More attention should be dedicated to studies of the thermodynamic stability of metal-doped $Ni_aX_b$ and $NiPX_3$ by accurate comparison of their band gap and referenced position of the Fermi level, as well as the role of electrolyte species on the thermodynamics of the conversion reaction. Picosecond scale *ab initio* molecular dynamic approaches will be highly useful for this purpose.

On the experimental side, a broader variety of metals should be considered for doping of $Ni_aX_b$ and $NiPX_3$ within the same conditions for comparison, including the accurate correction of their active surface area. A commonly accepted strategy, to increase the surface area of electrocatalysts through morphology changes, makes it more complicated to understand the true nature of the electrocatalytic activity/stability of the material, especially for foam-based electrocatalysts, as their electrochemical data corrected onto a geometric surface area might overestimate the real activity. The active surface area and active surface area normalized voltammetry data should be reported to accurately describe the trend in intrinsic activity and stability of different metal-doped nickel-based catalysts. It is compulsory to use a fixed metal doping ratio whenever accurate data for different metal-doped $Ni_aX_b$ and $NiPX_3$ is reported. Apart from that, it is preferably to compare as-synthesized crystals with the same dominant facet structure in order to avoid contribution of polycrystallinity in the electrocatalysts. In this regard, it makes sense to conduct more fundamental experimental studies on metal doping in nickel-based (phospho)-chalcogenide phases for bulk materials with the same symmetry of crystals or preferably in single crystal form. It will also be important to conduct additional studies for Cu, Ni, Co, Fe and Mn-based (phospho)chalcogenides/oxides, to understand the maximum difference in the oxophilicity of transition metals, which can enable efficient charge transport and bifunctionality in these systems. New precise experimental methods, as well as real-time testing to detect the true electrocatalytic activity and stability of the active site of the material, should be considered more often. A phase transformation upon metal doping and/or applied current might take place; therefore, the precise structure with its physical–chemical properties of newly formed phases (oxides, *etc.*) need to be examined carefully, at least using chelating agents, along with electrochemical testing which selectively reacts with metals in a particular oxidation state or more direct synchrotron-based techniques.

## Conflicts of interest

The author declares no competing financial interest.

## References

1 T. Ahmad and D. Zhang, *Energy Rep.*, 2020, **6**, 1973–1991.
2 N. Shen, R. Deng, H. Liao and O. Shevchuk, *Util. Policy*, 2020, **64**, 101055.
3 A. Ugurlu and S. Oztuna, *Int. J. Hydrogen Energy*, 2015, **40**, 11178–11188.
4 X. Zou and Y. Zhang, *Chem. Soc. Rev.*, 2015, **44**, 5148–5180.
5 J. Zhu, L. Hu, P. Zhao, L. Y. S. Lee and K.-Y. Wong, *Chem. Rev.*, 2020, **120**, 851–918.
6 M. Tahir, L. Pan, F. Idrees, X. Zhang, L. Wang, J.-J. Zou and Z. L. Wang, *Nano Energy*, 2017, **37**, 136–157.
7 B. Xiong, L. Chen and J. Shi, *ACS Catal.*, 2018, **8**, 3688–3707.
8 Y. Wang, B. Kong, D. Zhao, H. Wang and C. Selomulya, *Nano Today*, 2017, **15**, 26–55.

9 M. Gong, D.-Y. Wang, C.-C. Chen, B.-J. Hwang and H. Dai, *Nano Res.*, 2016, **9**, 28–46.
10 M. Gong and H. Dai, *Nano Res.*, 2015, **8**, 23–39.
11 Z. W. Seh, J. Kibsgaard, C. F. Dickens, I. Chorkendorff, J. K. Nørskov and T. F. Jaramillo, *Science*, 2017, **355**, eaad4998.
12 S. Klaus, Y. Cai, M. W. Louie, L. Trotochaud and A. T. Bell, *J. Phys. Chem. C*, 2015, **119**, 7243–7254.
13 C. Spöri, J. T. H. Kwan, A. Bonakdarpour, D. P. Wilkinson and P. Strasser, *Angew. Chem., Int. Ed.*, 2017, **56**, 5994–6021.
14 P. Wang, M. Yan, J. Meng, G. Jiang, L. Qu, X. Pan, J. Z. Liu and L. Mai, *Nat. Commun.*, 2017, **8**, 645.
15 J. Zaffran, M. B. Stevens, C. D. M. Trang, M. Nagli, M. Shehadeh, S. W. Boettcher and M. Caspary Toroker, *Chem. Mater.*, 2017, **29**, 4761–4767.
16 J. A. Arminio-Ravelo, A. W. Jensen, K. D. Jensen, J. Quinson and M. Escudero-Escribano, *ChemPhysChem*, 2019, **20**, 2956–2963.
17 F. Lu, M. Zhou, Y. Zhou and X. Zeng, *Small*, 2017, **13**, 1701931.
18 A. Ciechan, M. J. Winiarski and M. Samsel-Czekała, *Intermetallics*, 2013, **41**, 44–50.
19 J. R. Swierk, S. Klaus, L. Trotochaud, A. T. Bell and T. D. Tilley, *J. Phys. Chem. C*, 2015, **119**, 19022–19029.
20 J. Jiang, F. Sun, S. Zhou, W. Hu, H. Zhang, J. Dong, Z. Jiang, J. Zhao, J. Li, W. Yan and M. Wang, *Nat. Commun.*, 2018, **9**, 2885.
21 W. Gao, M. Yan, H.-Y. Cheung, Z. Xia, X. Zhou, Y. Qin, C.-Y. Wong, J. C. Ho, C.-R. Chang and Y. Qu, *Nano Energy*, 2017, **38**, 290–296.
22 D. Rakov, Y. Li, S. Niu and P. Xu, *J. Alloys Compd.*, 2018, **769**, 532–538.
23 D. Zhou, Z. Cai, Y. Jia, X. Xiong, Q. Xie, S. Wang, Y. Zhang, W. Liu, H. Duan and X. Sun, *Nanoscale Horiz.*, 2018, **3**, 532–537.
24 Y. Wang, R. Zhang, J. Li, L. Li and S. Lin, *Nanoscale Res. Lett.*, 2014, **9**, 46.
25 C. Tsai, K. Chan, J. K. Nørskov and F. Abild-Pedersen, *Surf. Sci.*, 2015, **640**, 133–140.
26 S. Anantharaj, S. Kundu and S. Noda, *J. Mater. Chem. A*, 2020, **8**, 4174–4192.
27 J. Luxa, Š. Cintl, L. Spejchalová, J.-Y. Lin and Z. Sofer, *ACS Appl. Energy Mater.*, 2020, **3**, 11992–11999.
28 J. Wang, X. Li, B. Wei, R. Sun, W. Yu, H. Y. Hoh, H. Xu, J. Li, X. Ge, Z. Chen, C. Su and Z. Wang, *Adv. Funct. Mater.*, 2020, **30**, 1908708.
29 F. Wang, T. A. Shifa, P. Yu, P. He, Y. Liu, F. Wang, Z. Wang, X. Zhan, X. Lou, F. Xia and J. He, *Adv. Funct. Mater.*, 2018, **28**, 1802151.
30 A. P. Tiwari, D. Kim, Y. Kim, O. Prakash and H. Lee, *Nano Energy*, 2016, **28**, 366–372.
31 C. C. Mayorga-Martinez, Z. Sofer, D. Sedmidubský, Š. Huber, A. Y. S. Eng and M. Pumera, *ACS Appl. Mater. Interfaces*, 2017, **9**, 12563–12573.
32 B. Song, K. Li, Y. Yin, T. Wu, L. Dang, M. Cabán-Acevedo, J. Han, T. Gao, X. Wang, Z. Zhang, J. R. Schmidt, P. Xu and S. Jin, *ACS Catal.*, 2017, **7**, 8549–8557.
33 Z. Liang, Z. Yang, J. Dang, J. Qi, H. Yuan, J. Gao, W. Zhang, H. Zheng and R. Cao, *Chem. – Eur. J.*, 2019, **25**, 621–626.
34 S. Wang, B. Xiao, S. Shen, K. Song, Z. Lin, Z. Wang, Y. Chen and W. Zhong, *Nanoscale*, 2020, **12**, 14459–14464.
35 J. Chang, G. Wang, A. Belharsa, J. Ge, W. Xing and Y. Yang, *Small Methods*, 2020, **4**, 1900632.
36 R. Gusmão, Z. Sofer and M. Pumera, *Adv. Funct. Mater.*, 2019, **29**, 1805975.
37 J. Yu, W.-J. Li, H. Zhang, F. Zhou, R. Li, C.-Y. Xu, L. Zhou, H. Zhong and J. Wang, *Nano Energy*, 2019, **57**, 222–229.
38 R. N. Jenjeti, R. Kumar and S. Sampath, *J. Mater. Chem. A*, 2019, **7**, 14545–14551.
39 A. Hashemi, H.-P. Komsa, M. Puska and A. V. Krasheninnikov, *J. Phys. Chem. C*, 2017, **121**, 27207–27217.
40 Y. V. Kuzminskii, B. M. Voronin and N. N. Redin, *J. Power Sources*, 1995, **55**, 133–141.
41 Y. Sang, L. Wang, X. Cao, G. Ding, Y. Ding, Y. Hao, N. Xu, H. Yu, L. Li and S. Peng, *J. Alloys Compd.*, 2020, **831**, 154775.
42 Q. Liang, Y. Zheng, C. Du, Y. Luo, J. Zhang, B. Li, Y. Zong and Q. Yan, *Small Methods*, 2017, **1**, 1700304.
43 Q. Liang, L. Zhong, C. Du, Y. Zheng, Y. Luo, J. Xu, S. Li and Q. Yan, *Adv. Funct. Mater.*, 2018, **28**, 1805075.
44 C.-F. Du, K. N. Dinh, Q. Liang, Y. Zheng, Y. Luo, J. Zhang and Q. Yan, *Adv. Energy Mater.*, 2018, **8**, 1801127.
45 R. Gusmão, Z. Sofer, D. Sedmidubský, Š. Huber and M. Pumera, *ACS Catal.*, 2017, **7**, 8159–8170.
46 R. Samal, G. Sanyal, B. Chakraborty and C. S. Rout, *J. Mater. Chem. A*, 2021, **9**, 2560–2591.
47 M. Zhu, H. Kou, K. Wang, H. Wu, D. Ding, G. Zhou and S. Ding, *Mater. Horiz.*, 2020, **7**, 3131–3160.
48 A. C. Garcia, T. Touzalin, C. Nieuwland, N. Perini and M. T. M. Koper, *Angew. Chem., Int. Ed.*, 2019, **58**, 12999–13003.
49 N. Mahmood, Y. Yao, J.-W. Zhang, L. Pan, X. Zhang and J.-J. Zou, *Adv. Sci.*, 2018, **5**, 1700464.
50 G. B. Darband, M. Aliofkhazraei and S. Shanmugam, *Renewable Sustainable Energy Rev.*, 2019, **114**, 109300.
51 D. Strmcnik, M. Uchimura, C. Wang, R. Subbaraman, N. Danilovic, D. van der Vliet, A. P. Paulikas, V. R. Stamenkovic and N. M. Markovic, *Nat. Chem.*, 2013, **5**, 300–306.
52 M. Görlin, M. Gliech, J. F. de Araújo, S. Dresp, A. Bergmann and P. Strasser, *Catal. Today*, 2016, **262**, 65–73.
53 T. Reier, H. N. Nong, D. Teschner, R. Schlögl and P. Strasser, *Adv. Energy Mater.*, 2017, **7**, 1601275.
54 C. C. L. McCrory, S. Jung, I. M. Ferrer, S. M. Chatman, J. C. Peters and T. F. Jaramillo, *J. Am. Chem. Soc.*, 2015, **137**, 4347–4357.
55 B. Zhang, X. Zheng, O. Voznyy, R. Comin, M. Bajdich, M. García-Melchor, L. Han, J. Xu, M. Liu, L. Zheng, F. P. García de Arquer, C. T. Dinh, F. Fan, M. Yuan, E. Yassitepe, N. Chen, T. Regier, P. Liu, Y. Li, P. De Luna, A. Janmohamed, H. L. Xin, H. Yang, A. Vojvodic and E. H. Sargent, *Science*, 2016, **352**, 333–337.
56 L. D. Wickramasinghe, R. Zhou, R. Zong, P. Vo, K. J. Gagnon and R. P. Thummel, *J. Am. Chem. Soc.*, 2015, **137**, 13260–13263.

57 Y. H. Wang, S. Zheng, W. M. Yang, R. Y. Zhou, Q. F. He, P. Radjenovic, J. C. Dong, S. Li, J. Zheng, Z. L. Yang, G. Attard, F. Pan, Z. Q. Tian and J. F. Li, *Nature*, 2021, **600**, 81–85.
58 M. S. Burke, L. J. Enman, A. S. Batchellor, S. Zou and S. W. Boettcher, *Chem. Mater.*, 2015, **27**, 7549–7558.
59 D. Mattia, M. P. Rossi, B. M. Kim, G. Korneva, H. H. Bau and Y. Gogotsi, *J. Phys. Chem. B*, 2006, **110**, 9850–9855.
60 J. Wang, J. Liu, B. Zhang, X. Ji, K. Xu, C. Chen, L. Miao and J. Jiang, *Phys. Chem. Chem. Phys.*, 2017, **19**, 10125–10132.
61 W. T. Hong, M. Risch, K. A. Stoerzinger, A. Grimaud, J. Suntivich and Y. Shao-Horn, *Energy Environ. Sci.*, 2015, **8**, 1404–1427.
62 N.-T. Suen, S.-F. Hung, Q. Quan, N. Zhang, Y.-J. Xu and H. M. Chen, *Chem. Soc. Rev.*, 2017, **46**, 337–365.
63 Y. Matsumoto and E. Sato, *Mater. Chem. Phys.*, 1986, **14**, 397–426.
64 P. Sen and R. K. Chouhan, *Electron. Struct.*, 2020, **2**, 25003.
65 J. Jin, J. Yin, H. Liu, B. Huang, Y. Hu, H. Zhang, M. Sun, Y. Peng, P. Xi and C. Yan, *Angew. Chem.*, 2021, **133**, 14236–14242.
66 J. Yin, J. Jin, M. Lu, B. Huang, H. Zhang, Y. Peng, P. Xi and C.-H. Yan, *J. Am. Chem. Soc.*, 2020, **142**, 18378–18386.
67 D. Jia, L. Han, Y. Li, W. He, C. Liu, J. Zhang, C. Chen, H. Liu and H. L. Xin, *J. Mater. Chem. A*, 2020, **8**, 18207–18214.
68 J. Wang, A. Yang, J. Li, K. Su, Y. Tang and X. Qiu, *Appl. Catal., B*, 2022, **300**, 120727.
69 Y. Ge, S.-P. Gao, P. Dong, R. Baines, P. M. Ajayan, M. Ye and J. Shen, *Nanoscale*, 2017, **9**, 5538–5544.
70 A. Long, W. Li, M. Zhou, W. Gao, B. Liu, J. Wei, X. Zhang, H. Liu, Y. Liu and X. Zeng, *J. Mater. Chem. A*, 2019, **7**, 21514–21522.
71 J. You, C. Si, J. Zhou and Z. Sun, *J. Phys. Chem. C*, 2019, **123**, 3719–3726.
72 S. R. Kadam, A. N. Enyashin, L. Houben, R. Bar-Ziv and M. Bar-Sadan, *J. Mater. Chem. A*, 2020, **8**, 1403–1416.
73 X. Chia, N. A. A. Sutrisnoh, Z. Sofer, J. Luxa and M. Pumera, *Chem. – Eur. J.*, 2018, **24**, 3199–3208.
74 Y. Song, X. Wang and W. Mi, *Phys. Rev. Mater.*, 2017, **1**, 74408.
75 H. B. Tao, L. Fang, J. Chen, H. Bin Yang, J. Gao, J. Miao, S. Chen and B. Liu, *J. Am. Chem. Soc.*, 2016, **138**, 9978–9985.
76 E. Fabbri, A. Habereder, K. Waltar, R. Kötz and T. J. Schmidt, *Catal. Sci. Technol.*, 2014, **4**, 3800–3821.
77 A. J. Bard and L. R. Faulkner, *Fundamentals and Applications*, Springer, New York, Wiley, 2002.
78 G. Fu, X. Wen, S. Xi, Z. Chen, W. Li, J.-Y. Zhang, A. Tadich, R. Wu, D.-C. Qi, Y. Du, J. Cheng and K. H. L. Zhang, *Chem. Mater.*, 2019, **31**, 419–428.
79 A. B. Laursen, A. S. Varela, F. Dionigi, H. Fanchiu, C. Miller, O. L. Trinhammer, J. Rossmeisl and S. Dahl, *J. Chem. Educ.*, 2012, **89**, 1595–1599.
80 A. J. Medford, A. Vojvodic, J. S. Hummelshøj, J. Voss, F. Abild-Pedersen, F. Studt, T. Bligaard, A. Nilsson and J. K. Nørskov, *J. Catal.*, 2015, **328**, 36–42.
81 H. L. Lord, W. Zhan and J. Pawliszyn, *Fundamentals and applications of needle trap devices*, 2012, vol. 2.
82 W. Luc, Z. Jiang, J. G. Chen and F. Jiao, *ACS Catal.*, 2018, **8**, 9327–9333.
83 Q. Sun, Y. Dong, Z. Wang, S. Yin and C. Zhao, *Small*, 2018, **14**, 1704137.
84 M. K. Kundu, R. Mishra, T. Bhowmik and S. Barman, *J. Mater. Chem. A*, 2018, **6**, 23531–23541.
85 D. Strmcnik, P. P. Lopes, B. Genorio, V. R. Stamenkovic and N. M. Markovic, *Nano Energy*, 2016, **29**, 29–36.
86 K. Li, D. Rakov, W. Zhang and P. Xu, *Chem. Commun.*, 2017, **53**, 8199–8202.
87 N. Q. Tran, V. Q. Bui, H. M. Le, Y. Kawazoe and H. Lee, *Adv. Energy Mater.*, 2018, **8**, 1702139.
88 B. Kim, T. Kim, K. Lee and J. Li, *ChemElectroChem*, 2020, **7**, 3578–3589.
89 Z. Fang, L. Peng, Y. Qian, X. Zhang, Y. Xie, J. J. Cha and G. Yu, *J. Am. Chem. Soc.*, 2018, **140**, 5241–5247.
90 Y. Li, Y. Gao, S. Yang, C. Wu and Y. Tan, *J. Mater. Chem. A*, 2020, **8**, 12013–12027.
91 J. Hu, A. Al-Salihy, J. Wang, X. Li, Y. Fu, Z. Li, X. Han, B. Song and P. Xu, *Adv. Sci.*, 2021, **8**, 2103314.
92 D. Rakov, C. Sun, Z. Lu, S. Li and P. Xu, *Adv. Energy Sustainable Res.*, 2021, **2**, 2100071.
93 X. Xu, F. Song and X. Hu, *Nat. Commun.*, 2016, **7**, 1–7.
94 T. X. Nguyen, Y. Su, C. Lin and J. Ting, *Adv. Funct. Mater.*, 2021, **31**, 2106229.
95 O. Mabayoje, A. Shoola, B. R. Wygant and C. B. Mullins, *ACS Energy Lett.*, 2016, **1**, 195–201.
96 Q. Chen, L. Huang, Q. Kong, X. An, X. Wu, W. Yao and C. Sun, *J. Electroanal. Chem.*, 2022, **907**, 116047.
97 C.-Z. Yuan, Y.-F. Jiang, Z. Wang, X. Xie, Z.-K. Yang, A. Bin Yousaf and A.-W. Xu, *J. Mater. Chem. A*, 2016, **4**, 8155–8160.
98 Z. Liu, G. Zhang, K. Zhang, H. Liu and J. Qu, *ACS Sustainable Chem. Eng.*, 2018, **6**, 7206–7211.
99 V. Grasso, S. Santangelo and M. Piacentini, *Solid State Ionics*, 1986, **20**, 9–15.
100 Y. Ohno and K. Hirama, *J. Solid State Chem.*, 1986, **63**, 258–266.
101 D. Mukherjee, P. M. Austeria and S. Sampath, *ACS Appl. Energy Mater.*, 2018, **1**, 220–231.
102 J. Yang, Y. Zhou, Q. Guo, Y. Dedkov and E. Voloshina, *RSC Adv.*, 2020, **10**, 851–864.
103 Z. Liu, Y. Wang, R. Chen, C. Chen, H. Yang, J. Ma, Y. Li and S. Wang, *J. Power Sources*, 2018, **403**, 90–96.
104 J. Zhuo, M. Cabán-Acevedo, H. Liang, L. Samad, Q. Ding, Y. Fu, M. Li and S. Jin, *ACS Catal.*, 2015, **5**, 6355–6361.
105 G.-F. Chen, T. Y. Ma, Z.-Q. Liu, N. Li, Y.-Z. Su, K. Davey and S.-Z. Qiao, *Adv. Funct. Mater.*, 2016, **26**, 3314–3323.
106 V. Zhukov, S. Alvarez and D. Novikov, *J. Phys. Chem. Solids*, 1996, **57**, 647–652.
107 B. Qiu, L. Cai, Y. Wang, Z. Lin, Y. Zuo, M. Wang and Y. Chai, *Adv. Funct. Mater.*, 2018, **28**, 1706008.
108 S. Fu, C. Zhu, J. Song, M. H. Engelhard, X. Li, D. Du and Y. Lin, *ACS Energy Lett.*, 2016, **1**, 792–796.
109 S. Shanmugam, A. Sivanantham, M. Matsunaga, U. Simon and T. Osaka, *Electrochim. Acta*, 2019, **297**, 749–754.

110 S. Y. Kim, T. Y. Kim, L. J. Sandilands, S. Sinn, M.-C. Lee, J. Son, S. Lee, K.-Y. Choi, W. Kim and B.-G. Park, *Phys. Rev. Lett.*, 2018, **120**, 136402.
111 C.-H. Ho, T.-Y. Hsu and L. C. Muhimmah, *npj 2D Mater. Appl.*, 2021, **5**, 1–10.
112 M. Yan, Y. Jin, Z. Wu, A. Tsaturyan, A. Makarova, D. Smirnov, E. Voloshina and Y. Dedkov, *J. Phys. Chem. Lett.*, 2021, **12**, 2400–2405.
113 N. Kurita and K. Nakao, *J. Phys. Soc. Jpn.*, 1989, **58**, 232–243.
114 Y.-Z. Xu, C.-Z. Yuan, Z.-W. Liu and X.-P. Chen, *Catal. Sci. Technol.*, 2018, **8**, 128–133.
115 C.-F. Du, N. D. Khang, Q. Liang, Y. Zheng, Y. Luo, J. Zhang and Q. Yan, *Adv. Energy Mater.*, 2018, **8**, 1801127, DOI: **10.1002/aenm.201801127**.
116 A. Jawaid, D. Nepal, K. Park, M. Jespersen, A. Qualley, P. Mirau, L. F. Drummy and R. A. Vaia, *Chem. Mater.*, 2016, **28**, 337–348.
117 E. D. Grayfer, M. N. Kozlova and V. E. Fedorov, *Adv. Colloid Interface Sci.*, 2017, **245**, 40–61.
118 B. Konkena, J. Masa, A. J. R. Botz, I. Sinev, W. Xia, J. Koßmann, R. Drautz, M. Muhler and W. Schuhmann, *ACS Catal.*, 2017, **7**, 229–237.
119 A. Kuhn, L. M. Schoop, R. Eger and B. V. Lotsch, *Z. Anorg. Allg. Chem.*, 2016, **642**, 356–360.
120 D. Tripathy and S. Sampath, *J. Power Sources*, 2020, **478**, 229066.
121 R. Wang, J. Huang, X. Zhang, J. Han, Z. Zhang, T. Gao, L. Xu, S. Liu, P. Xu and B. Song, *ACS Nano*, 2022, **16**, 3593–3603.
122 K. Alam, T. Das, S. Chakraborty and P. Sen, *Phys. Chem. Chem. Phys.*, 2021, **23**, 23967–23977.
123 H. Sun, X. Xu, Y. Song, W. Zhou and Z. Shao, *Adv. Funct. Mater.*, 2021, **31**, 2009779.
124 Z. Xiao, L. Yan, Q. Hu, B. Xiang, Y. Wang, J. Hao, X. Zou, W. Li and S. Wei, *Dalton Trans.*, 2022, **51**, 8318–8326.
125 R. E. N. Jun, J.-G. Wang, J.-F. Li and Y.-W. Li, *J. Fuel Chem. Technol.*, 2007, **35**, 458–464.
126 D. Zhang, X. Zhou, J. Liu, L. Dong, J. Zhao, Y. Xie and W. Sun, *Mater. Sci. Eng., B*, 2021, **273**, 115389.
127 H. Liang, A. N. Gandi, D. H. Anjum, X. Wang, U. Schwingenschlögl and H. N. Alshareef, *Nano Lett.*, 2016, **16**, 7718–7725.
128 D. Liu, H. Ai, M. Chen, P. Zhou, B. Li, D. Liu, X. Du, K. H. Lo, K. Ng and S. Wang, *Small*, 2021, **17**, 2007557.
129 Q. Liang, L. Zhong, C. Du, Y. Luo, Y. Zheng, S. Li and Q. Yan, *Nano Energy*, 2018, **47**, 257–265.
130 F. Dionigi and P. Strasser, *Adv. Energy Mater.*, 2016, **6**, 1600621.
131 R. Subbaraman, D. Tripkovic, K.-C. Chang, D. Strmcnik, A. P. Paulikas, P. Hirunsit, M. Chan, J. Greeley, V. Stamenkovic and N. M. Markovic, *Nat. Mater.*, 2012, **11**, 550–557.
132 S.-S. Sun, *J. Mater. Sci.: Mater. Electron.*, 2007, **18**, 1143–1146.
133 T.-W. Wang, T.-L. Wang, W.-J. Chou, L.-F. Wu and S.-H. Lin, *Phys. Chem. Chem. Phys.*, 2021, **23**, 2305–2312.
134 H. Liu, J. Zhou, L. Zhang, Z. Hu, C. Kuo, J. Li, Y. Wang, L. H. Tjeng, T.-W. Pi, A. Tanaka, L. Song, J.-Q. Wang and S. Zhang, *J. Phys. Chem. C*, 2017, **121**, 16079–16087.
135 M. N. Grisolia, J. Varignon, G. Sanchez-Santolino, A. Arora, S. Valencia, M. Varela, R. Abrudan, E. Weschke, E. Schierle, J. E. Rault, J. P. Rueff, A. Barthélémy, J. Santamaria and M. Bibes, *Nat. Phys.*, 2016, **12**, 484–492.
136 L. Yu, J. Zhang, Y. Dang, J. He, Z. Tobin, P. Kerns, Y. Dou, Y. Jiang, Y. He and S. L. Suib, *ACS Catal.*, 2019, **9**, 6919–6928.
137 H. Li, G. Gao, H. Zhao, W. Wang, Y. Yang, Y. Du, S. Li, Y. Liu and L. Wang, *Int. J. Hydrogen Energy*, 2021, **46**, 33078–33086.
138 A. Aruchamy, H. Berger and F. Lévy, *J. Electrochem. Soc.*, 1989, **136**, 2261.
139 Y. Sun, A. Huang, Z. Li, Y.-Q. Fu and Z. Wang, *Electrocatalysis*, 2022, **13**, 494–501.
140 M. Khodabakhshi, S. Chen, T. Ye, H. Wu, L. Yang, W. Zhang and H. Chang, *ACS Appl. Mater. Interfaces*, 2020, **12**, 36268–36276.
141 J. Xu, J. Li, D. Xiong, B. Zhang, Y. Liu, K.-H. Wu, I. Amorim, W. Li and L. Liu, *Chem. Sci.*, 2018, **9**, 3470–3476.
142 D. Mukherjee, P. M. Austeria and S. Sampath, *ACS Energy Lett.*, 2016, **1**, 367–372.
143 P. Liu and Y. Pu, *Int. J. Hydrogen Energy*, 2022, **47**, 197–202.
144 N. Jiang, Q. Tang, M. Sheng, B. You, D. Jiang and Y. Sun, *Catal. Sci. Technol.*, 2016, **6**, 1077–1084.
145 D. Y. Chung, J. W. Han, D.-H. Lim, J.-H. Jo, S. J. Yoo, H. Lee and Y.-E. Sung, *Nanoscale*, 2015, **7**, 5157–5163.
146 J. Zhu and Y. Ni, *CrystEngComm*, 2018, **20**, 3344–3352.
147 J. Masud, M. Nath, U. De Silva and D. Allada, *ECS Meet. Abstr*, 2018, (29), 1674, DOI: **10.1149/ma2018-01/29/1674**.
148 K. S. Bhat and H. S. Nagaraja, *Mater. Res. Innovations*, 2021, **25**, 29–52.
149 D. Kong, J. J. Cha, H. Wang, H. R. Lee and Y. Cui, *Energy Environ. Sci.*, 2013, **6**, 3553–3558.
150 M. S. Faber, M. A. Lukowski, Q. Ding, N. S. Kaiser and S. Jin, *J. Phys. Chem. C*, 2014, **118**, 21347–21356.
151 C. Yu, H. Huang, S. Zhou, X. Han, C. Zhao, J. Yang, S. Li, W. Guo, B. An, J. Zhao and J. Qiu, *Nano Res.*, 2018, **11**, 3411–3418.
152 Y. Du, G. Cheng and W. Luo, *Catal. Sci. Technol.*, 2017, **7**, 4604–4608.
153 G. Kalaiyarasan, K. Aswathi and J. Joseph, *Int. J. Hydrogen Energy*, 2017, **42**, 22866–22876.
154 Y. Wang, N. Chen, X. Du, X. Han and X. Zhang, *J. Alloys Compd.*, 2022, **893**, 162269.
155 T. A. Bither, R. J. Bouchard, W. H. Cloud, P. C. Donohue and W. J. Siemons, *Inorg. Chem.*, 1968, **7**, 2208–2220.
156 S. Suga, K. Inoue, M. Taniguchi, S. Shin, M. Seki, K. Sato and T. Teranishi, *J. Phys. Soc. Jpn.*, 1983, **52**, 1848–1856.
157 J.-Q. Chi, K.-L. Yan, Z. Xiao, B. Dong, X. Shang, W.-K. Gao, X. Li, Y.-M. Chai and C.-G. Liu, *Int. J. Hydrogen Energy*, 2017, **42**, 20599–20607.
158 Y. Du, G. Cheng and W. Luo, *Catal. Sci. Technol.*, 2017, **7**, 4604–4608.
159 X. Wang, Y. Zhou, M. Liu, C. Chen and J. Zhang, *Electrochim. Acta*, 2019, **297**, 197–205.
160 X. Cao, Y. Hong, N. Zhang, Q. Chen, J. Masud, M. A. Zaeem and M. Nath, *ACS Catal.*, 2018, **8**, 8273–8289.

161 A. Shankar, R. Elakkiya and G. Maduraiveeran, *New J. Chem.*, 2020, **44**, 5071–5078.
162 X. He, X. Zhao, F. Yin, B. Chen, G. Li and H. Yin, *Int. J. Energy Res.*, 2020, **44**, 7057–7067.
163 X. Luan, H. Du, Y. Kong, F. Qu and L. Lu, *Chem. Commun.*, 2019, **55**, 7335–7338.
164 W. Zheng, M. Liu and L. Y. S. Lee, *ACS Energy Lett.*, 2020, **5**, 3260–3264.
165 E. Cossar, M. S. E. Houache, Z. Zhang and E. A. Baranova, *J. Electroanal. Chem.*, 2020, **870**, 114246.
166 M.-H. Wu, W.-J. Chou, J.-S. Huang, D. B. Putungan and S.-H. Lin, *Phys. Chem. Chem. Phys.*, 2019, **21**, 21561–21567.
167 R. Gómez-Balderas, R. Oviedo-Roa, J. M. Martínez-Magadán, C. Amador and D. A. Dixon, *Surf. Sci.*, 2002, **518**, 163–173.
168 D. Liang, J. Mao, P. Liu, J. Li, J. Yan and W. Song, *Int. J. Hydrogen Energy*, 2020, **45**, 27047–27055.
169 J. Yin, J. Jin, H. Zhang, M. Lu, Y. Peng, B. Huang, P. Xi and C.-H. Yan, *Angew. Chem., Int. Ed.*, 2019, **58**, 18676–18682.
170 Y.-Z. Xu, C.-Z. Yuan and X.-P. Chen, *RSC Adv.*, 2016, **6**, 106832–106836.
171 Q. Wang, P. Liu, Y. Liu, X. Peng, Y.-L. Men, Y.-B. Li and Y.-X. Pan, *Ind. Eng. Chem. Res.*, 2019, **58**, 22977–22983.
172 L. Jiang, N. Yang, C. Yang, X. Zhu, Y. Jiang, X. Shen, C. Li and Q. Sun, *Appl. Catal., B*, 2020, **269**, 118780.
173 H. Li, S. Chen, Y. Zhang, Q. Zhang, X. Jia, Q. Zhang, L. Gu, X. Sun, L. Song and X. Wang, *Nat. Commun.*, 2018, **9**, 2452.
174 P. Farinazzo Bergamo Dias Martins, P. Papa Lopes, E. A. Ticianelli, V. R. Stamenkovic, N. M. Markovic and D. Strmcnik, *Electrochem. Commun.*, 2019, **100**, 30–33.
175 J. Yan, H. Wu, P. li, H. Chen, R. Jiang and S. (Frank) Liu, *J. Mater. Chem. A*, 2017, **5**, 10173–10181.
176 B. Fei, Z. Chen, J. Liu, H. Xu, X. Yan, H. Qing, M. Chen and R. Wu, *Adv. Energy Mater.*, 2020, **10**, 2001963.
177 S. Dutta, A. Indra, Y. Feng, T. Song and U. Paik, *ACS Appl. Mater. Interfaces*, 2017, **9**, 33766–33774.
178 Z. Zou, X. Wang, J. Huang, Z. Wu and F. Gao, *J. Mater. Chem. A*, 2019, **7**, 2233–2241.
179 T. Wang, D. Gao, W. Xiao, P. Xi, D. Xue and J. Wang, *Nano Res.*, 2018, **11**, 6051–6061.
180 W. Dai, Y. Pan, K. Ren, Y. Zhu and T. Lu, *Electrochim. Acta*, 2020, **355**, 136821.
181 G. Zhang, Y.-S. Feng, W.-T. Lu, D. He, C.-Y. Wang, Y.-K. Li, X.-Y. Wang and F.-F. Cao, *ACS Catal.*, 2018, **8**, 5431–5441.
182 L. Lv, Z. Li, K.-H. Xue, Y. Ruan, X. Ao, H. Wan, X. Miao, B. Zhang, J. Jiang, C. Wang and K. (Ken) Ostrikov, *Nano Energy*, 2018, **47**, 275–284.
183 M. B. Stevens, C. D. M. Trang, L. J. Enman, J. Deng and S. W. Boettcher, *J. Am. Chem. Soc.*, 2017, **139**, 11361–11364.
184 B. M. Hunter, N. B. Thompson, A. M. Müller, G. R. Rossman, M. G. Hill, J. R. Winkler and H. B. Gray, *Joule*, 2018, **2**, 747–763.
185 Y. Gong, Y. Zhi, Y. Lin, T. Zhou, J. Li, F. Jiao and W. Wang, *Dalton Trans.*, 2019, **48**, 6718–6729.
186 X. Wang, H. Tian, M. Pi, D. Zhang and S. Chen, *Int. J. Hydrogen Energy*, 2020, **45**, 12237–12243.
187 H.-W. Man, C.-S. Tsang, M. M.-J. Li, J. Mo, B. Huang, L. Y. S. Lee, Y. Leung, K.-Y. Wong and S. C. E. Tsang, *Chem. Commun.*, 2018, **54**, 8630–8633.
188 H.-W. Man, C.-S. Tsang, M. M.-J. Li, J. Mo, B. Huang, L. Y. S. Lee, Y. Leung, K.-Y. Wong and S. C. E. Tsang, *Appl. Catal., B*, 2019, **242**, 186–193.
189 M. Wang, W. Fu, L. Du, Y. Wei, P. Rao, L. Wei, X. Zhao, Y. Wang and S. Sun, *Appl. Surf. Sci.*, 2020, **515**, 146059.
190 L. Zeng, Z. Liu, K. Sun, Y. Chen, J. Zhao, Y. Chen, Y. Pan, Y. Lu, Y. Liu and C. Liu, *J. Mater. Chem. A*, 2019, **7**, 25628–25640.
191 A. Manikandan, E. Hema, M. Durka, M. Amutha Selvi, T. Alagesan and S. Arul Antony, *J. Inorg. Organomet. Polym. Mater.*, 2015, **25**, 804–815.
192 L. Zeng, K. Zhou, L. Yang, G. Du, L. Liu and W. Zhou, *ACS Appl. Energy Mater.*, 2018, **1**, 6279–6287.
193 C. Qin, A. Fan, D. Ren, C. Luan, J. Yang, Y. Liu, X. Zhang, X. Dai and M. Wang, *Electrochim. Acta*, 2019, **323**, 134756.
194 N. Chen, Y. Wang, X. Du and X. Zhang, *Dalton Trans.*, 2021, **50**, 2964–2972.
195 J.-J. Duan, Z. Han, R.-L. Zhang, J.-J. Feng, L. Zhang, Q.-L. Zhang and A.-J. Wang, *J. Colloid Interface Sci.*, 2021, **588**, 248–256.
196 J.-F. Qin, M. Yang, S. Hou, B. Dong, T.-S. Chen, X. Ma, J.-Y. Xie, Y.-N. Zhou, J. Nan and Y.-M. Chai, *Appl. Surf. Sci.*, 2020, **502**, 144172.
197 M. A. Ashraf, C. Li, B. T. Pham and D. Zhang, *Int. J. Hydrogen Energy*, 2020, **45**, 24670–24683.
198 M. Cui, C. Yang, B. Li, Q. Dong, M. Wu, S. Hwang, H. Xie, X. Wang, G. Wang and L. Hu, *Adv. Energy Mater.*, 2021, **11**, 2002887.
199 F. Zeng, C. Broicher, J. P. Hofmann, S. Palkovits and R. Palkovits, *ChemCatChem*, 2020, **12**, 710–716.
200 W. Wen, X. Du and X. Zhang, *J. Alloys Compd.*, 2022, **918**, 165739.
201 X. Du, G. Ma and X. Zhang, *ACS Sustainable Chem. Eng.*, 2019, **7**, 19257–19267.
202 W. Xu, Z. Lu, X. Sun, L. Jiang and X. Duan, *Acc. Chem. Res.*, 2018, **51**, 1590–1598.
203 X. Shan, J. Liu, H. Mu, Y. Xiao, B. Mei, W. Liu, G. Lin, Z. Jiang, L. Wen and L. Jiang, *Angew. Chem., Int. Ed.*, 2020, **59**, 1659–1665.